

Mechanism of Bismuth Stimulated Bottom-up Gold Feature Filling

D. Josell, T.M. Braun, and T.P. Moffat

Materials Science and Engineering Division

National Institute of Standards and Technology

Gaithersburg, MD, USA

ABSTRACT

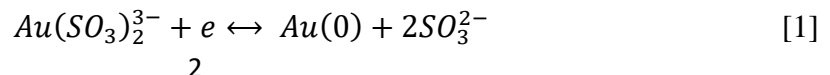
The mechanism underlying Bi^{3+} -stimulated bottom-up Au filling and self-passivation in trenches and vias in slightly alkaline $Na_3Au(SO_3)_2 + Na_2SO_3$ electrolytes is explored. The impacts of electrolyte components $Na_3Au(SO_3)_2$, Na_2SO_3 and Bi^{3+} and potential-dependent kinetic factors on the rate of Au electrodeposition are quantified experimentally. Derived parameters are applied within the surfactant conservation Curvature Enhanced Accelerator Coverage model to simulate the filling of high aspect ratio trenches. It is observed that Bi adsorption accelerates the Au deposition rate with a non-linear dependence occurring around a critical coverage. Further, the impact of electrolyte composition is such that gradients of $Au(SO_3)_2^{3-}$ and SO_3^{2-} derived from reduction of $Au(SO_3)_2^{3-}$ during deposition accentuate deposition farther from the feature opening. These factors and surface area reduction at the bottoms of filling features localize active deposition to feature bottoms. Ultimately, weakening of the concentration gradients and associated kinetics as bottom-up feature filling progresses reduces the Bi coverage on the growth front below the critical value and bottom-up growth terminates. Good agreement is observed with key experimental features including the incubation period of conformal deposition, transition to

bottom-up growth, subsequent bottom-up filling and finally self-passivation as the growth front nears the field.

INTRODUCTION

Bottom-up superconformal gold electrodeposition in a sulfite electrolyte containing Bi^{3+} additive has been detailed in a series of recent reports¹⁻⁸. These studies detail filling of recessed features on metallized substrates including trenches, vias and fractal patterns followed by self-termination of the growth process with little further deposition, or overburden, on the overlying field. Feature filling in high aspect ratio trenches and vias as well as the associated Bi adsorption kinetics and deposit microstructure were explored. The process was shown to be particularly useful for the fabrication of dense, void-free high aspect ratio Au/Si gratings for X-ray interferometry and phase-contrast imaging applications for which the high absorption contrast between the Au-filled features and surrounding Si is especially well-suited⁹⁻¹⁵. Void-free, bottom-up filling was demonstrated in one-dimensional trench arrays as shallow as 3 μm to as deep as 305 μm with aspect ratio (depth/width) as low as 1.5 to greater than 60. Uniform filling in even the most aggressive features was demonstrated on gratings patterned across 100 mm Si wafers. The Au-filled gratings were applied to X-ray phase contrast imaging of biological samples, demonstrating the potential for broader biomedical applications such as have been explored using gratings filled by other processes.¹⁶⁻²¹

In the absence of additives, Au deposition from $Na_3Au(SO_3)_2 + Na_2SO_3$ electrolytes yields slow, nominally conformal but locally rough coatings in accord with the reaction stoichiometry



The reaction is typically performed in near neutral, slightly alkaline pH where $Au(SO_3)_2^{3-}$ and SO_3^{2-} are the dominant anions.²² In more acidic environments HSO_3^- becomes significant, leading to destabilization of the electrolyte. Gold deposition in the neat electrolyte is inhibited by adsorption of sulfite and its dimerization product $S_2O_5^{2-}$ with formation of the latter associated with the growth of optically rough films. Molecular additives, such as hydroxyethylene disphosphonic acid (HEDP), that interfere with sulfite dimerization are observed to facilitate the deposition of bright Au films.²³ Furthermore, the heavy metal p-block ion additives Tl^+ , Pb^{2+} and Bi^{3+} , reduced to their elemental form, strongly accelerate the Au deposition rate by altering the intrinsic blocking character of the sulfite based adlayer to also yield bright and smooth Au films. Analogous effects have been noted for cyanide electrolytes.²⁴ The use of Tl^+ combined with pulse plating can lead to improvements in the uniformity and smoothness of Au deposits²⁵⁻²⁹, while Pb^{2+} additions help attenuate roughness and even give rise to superconformal feature filling in trenches of modest aspect ratio³⁰⁻³². In both cases the filling dynamics are influenced by surfactant conservation during surface area change that necessarily accompanies the motion of non-planar surfaces. Smoothing has also been observed in the presence of $Bi_2(SO_4)_2$ additive.³³ However, in an even more dramatic fashion, Bi^{3+} additions can provide highly non-linear acceleration and bottom-up feature filling as detailed in prior experimental studies.¹⁻⁸ The strong bottom-up filling dynamic exhibits similarities to morphological evolution seen with certain deposition-suppressing additives. However, for those examples, feature filling is associated with depletion of the suppressor away from feature openings due to its consumption within the deposit.³⁴⁻³⁹ More importantly, the growth front and resulting microstructure in the Au systems³⁷⁻³⁹ tend to resemble those of additive-free deposition, which are distinctly inferior to the smooth compact deposits provided by Bi^{3+} additions.

Four distinctive and important characteristics of void-free filling in the Bi^{3+} -containing electrolyte are: 1) an “incubation period” of conformal deposition, 2) subsequent activation of deposition localized to the bottom surface of features, 3) continuing bottom-up deposition that yields void-free filling and 4) self-passivation of the active growth front at a distance from the feature opening defined by operating conditions. The experimental studies explored the duration and evolution of these four stages as functions of electrolyte concentrations, pH, applied potential and/or current, feature dimensions and convective transport conditions for electrolytes including (0.08, 0.16 and 0.32) $\text{mol}\cdot\text{L}^{-1}$ $Na_3Au(SO_3)_2$ + (0.32, 0.64 and 1.28) $\text{mol}\cdot\text{L}^{-1}$ Na_2SO_3 of pH 9.0 to 11.5 containing $1\ \mu\text{mol}\cdot\text{L}^{-1}$ to $50\ \mu\text{mol}\cdot\text{L}^{-1}$ Bi^{3+} . In these electrolytes and starting from relatively negative potentials, a positive shift of the deposition potential is generally accompanied by a transition from (i) subconformal feature filling, exhibiting a keyhole shaped void starting at the bottom of a given size feature, to (ii) “truncated bottom-up filling” with limited bottom-up deposition followed by activation of a portion of the upper sidewalls, manifest in a keyhole shaped void beginning some distance above the feature bottom, to (iii) entirely void-free, bottom-up filling to (iv) conformal filling until seam formation. These transitions in the feature filling geometry are observed to occur at less negative applied potentials during filling of deeper features, the positive shift of potential also increasing the incubation period from minutes at the more negative potentials that yield void-free filling of the lowest aspect ratio (1.5) and shallowest ($3\ \mu\text{m}$) features^{1,2} to hours and days at the more positive potentials required for void-free filling of the highest aspect ratio (>65) and deepest ($> 300\ \mu\text{m}$) features filled to date^{6,7}.

The present work quantitatively explores the interplay between Bi^{3+} -stimulated Au deposition and the constraints associated with deposition in recessed features to reveal the reaction dynamics that underlie the extreme bottom-up Au filling process. Two key elements are the threshold-like

dependence of the Au deposition rate on the Bi^{3+} coverage and the impact of electrolyte composition and applied potential on the rate of Bi^{3+} adsorption and, thereby, on the rate of Au deposition. Positive feedback develops from perturbation of the interfacial concentrations due to Au deposition from the $Au(SO_3)_2^{3-}$ complex and release of SO_3^{2-} during its reduction that create gradients of concentration within filling features. On net these changes increase the kinetics of Bi^{3+} adsorption and thus the coverage of adsorbed Bi and rate of Au deposition farther from the feature opening. This effect is accentuated in higher aspect ratio trenches. Localization of deposition underlying the bottom-up growth dynamic is further reinforced by local increase of the coverage of surfactant adsorbate that accompanies decrease of the surface area at the bottoms of filling features during Au deposition, i.e., the Curvature Enhanced Accelerator Coverage Mechanism (CEAC).⁴⁰⁻⁴⁵ The feedback between decreasing area and locally enhanced adsorbate coverage, and thereby accelerated Au deposition rate, is sustained during filling of the high aspect ratio trenches. However, net desorption of the Bi adsorbate as the growth front approaches the bulk electrolyte concentrations higher in the trench, combined with ongoing adsorbate burial in the deposit and any dilation of the surface as it approaches the field reduces the coverage to a steady state value below the threshold “critical” value required for accelerated deposition. Active deposition in filling features thereby ceases near the feature opening upon completion of filling.

The kinetics of Bi^{3+} adsorption and impact of the Bi adsorbate on the rate of Au deposition are herein assessed experimentally using chronoamperometric experiments on a rotating disk electrode (RDE). The observations, as well as previous comparison of chronoamperometry and Bi adsorbate coverage²⁻⁴, point to a critical or threshold Bi coverage at which the rate of Au deposition accelerates sharply. The impact of the $Au(SO_3)_2^{3-}$ and SO_3^{2-} concentrations and applied potential on the duration of the incubation period that precedes activation of Au deposition on the RDE

surface is summarized and a constitutive equation thereby developed for the rate constant of Bi^{3+} electroadsorption to Bi. The hyperbolic tangent function is used to simulate the nonlinear dependence of the Au deposition rate on Bi coverage; however, many logistic-like functions exhibiting nonlinear increase would yield qualitatively similar results. The coverage dependent interface reaction is coupled with equations accounting for Bi^{3+} adsorption from the electrolyte, Bi desorption back into the electrolyte, Bi burial in the deposit and change of Bi coverage with area change (CEAC mechanism). These are tied to standard mass and electrical transport equations within the electrolyte phase, including the impact of ohmic electrolyte losses on the reaction overpotential for both Bi adsorption and Au deposition. The equations are solved using finite difference computations within COMSOL. The trench filling simulations are found to be in good agreement with experimentally observed behaviors.

EXPERIMENTAL

GOLD ELECTRODEPOSITION

Au electrodeposition experiments were conducted at room temperature in a three-electrode electrochemical cell containing 40 mL of electrolyte. Potentials were measured relative to a Hg/Hg₂SO₄/saturated K₂SO₄ reference electrode (SSE) separated from the main cell by a Vycor fritted bridge. The electrolytes were all derived from a 0.32 mol·L⁻¹ Na₃Au(SO₃)₂ source solution (Technic Gold 25-F replenisher concentrate) in addition to a specified concentration of Na₂SO₃ salt diluted to the desired concentration with 18 MΩ·cm water. The Bi^{3+} additive was introduced by anodic dissolution of 99.999 mass % fused Bi metal electrode on the assumption of a 100 % efficient $Bi \Rightarrow Bi^{3+} + 3e^-$ dissolution reaction at -0.58 V SSE. Development of a surface tarnish

with dissolution suggests some increment of the charge goes to oxide formation, making the stated Bi^{3+} concentrations upper bounds. Although uncertainty in the absolute Bi^{3+} concentration exists, variation between the different electrolytes examined in this study was minimized by dosing from a single Bi^{3+} master solution. The master dosing electrolyte was $0.32 \text{ mol}\cdot\text{L}^{-1} Na_3Au(SO_3)_2$ with $100 \text{ }\mu\text{mol}\cdot\text{L}^{-1} Bi^{3+}$. The pH of the as-mixed electrolytes was in the range 9.2 to 9.6 as measured by a pH meter calibrated using pH 7.00 and 10.01 buffer solutions. As warranted, the pH was adjusted down using H_2SO_4 (prediluted in distilled water to avoid gold precipitation) and up using $NaOH$ (dissolved in distilled water for greater control).

Chronoamperometric experiments were conducted using a 0.5 cm diameter Au-coated Pt RDE whose surface was prepared before each experiment using 1200 grit silicon carbide paper. Experiments in each electrolyte were limited in number and duration to minimize both metal ion consumption from electrodeposition and acidification of the electrolyte due to oxidation of sulfite to sulfate at the Pt anode. In light of the previously observed impact of pH on Bi^{3+} adsorption kinetics⁴ the pH was monitored and adjusted back to 9.0 as required (pH deviations were typically < 0.05). No attempt was made to compensate for ohmic losses from the applied potential associated with current flow between the working and reference electrodes given that the deposition currents remained below 0.5 mA during the transients.

RESULTS

Electrochemical Measurements on a Planar Au-coated RDE

Previous studies utilized electroanalytical measurements on Au-coated RDEs in combination with feature filling experiments on patterned specimens to facilitate identification of conditions compatible with void-free processing in the Bi^{3+} -containing Au electrolytes. Cyclic voltammetry

and chronoamperometry were used to assess the impact of RDE rotation rate, pH and $Na_3Au(SO_3)_2$ and Bi^{3+} concentrations^{1,4,6}; the electrolytes examined all contained $0.64 \text{ mol}\cdot\text{L}^{-1}$ Na_2SO_3 as supporting electrolyte. Cyclic voltammetry exhibited diffusion-limited current density i_L at large overpotentials that doubled as four-fold increases of the RDE rotation rate halved the thickness δ of the diffusional boundary layer. However, limiting currents deviated below a simple linear dependence, $i_L = D_{Au(SO_3)_2} C_{Au(SO_3)_2} / \delta$, on the concentration $C_{Au(SO_3)_2}$ of the gold sulfite complex ion (hereafter called C_{Au}) assuming a fixed diffusion coefficient $D_{Au(SO_3)_2}$ (hereafter called D_{Au}) that most likely reflects an increase in viscosity with C_{Au} .⁶ Chronoamperometry was used to explore the impact of RDE rotation rate and electrolyte pH on the incubation period for active gold deposition.^{1,4}

Herein the effects of $Na_3Au(SO_3)_2$, Na_2SO_3 and Bi^{3+} concentrations on the incubation period are characterized further. Transients are shown in **Fig. 1** for Au deposition at four potentials for fixed concentrations of $Na_3Au(SO_3)_2$ and Na_2SO_3 while the Bi^{3+} concentration is varied from $3 \mu\text{mol}\cdot\text{L}^{-1}$ to $50 \mu\text{mol}\cdot\text{L}^{-1}$. Analogous transients were obtained to characterize the dependence on the $Na_3Au(SO_3)_2$ and Na_2SO_3 concentrations (not shown). The distinct transition from passive to active deposition is parameterized in terms of the incubation period, defined here as the time t_{inc} required to reach $1 \text{ mA}\cdot\text{cm}^{-2}$, based on the projected area of the planar RDE, with results summarized for the different Bi^{3+} concentrations and potentials in **Fig. 1f**. The chronoamperometric transients were terminated after reaching values in the range (2 to 3) $\text{mA}\cdot\text{cm}^{-2}$, which correspond to only partial activation of the RDE surface. Because the majority of transients integrate to a charge of less than 0.1 C, and even the longest integrate to less than 0.2 C, the total deposition charge in each electrolyte was readily kept below 1 % of the Au equivalent in

solution, thereby minimizing the cumulative impact of reactant depletion on successive experiments.

Incubation Period

The sharp transitions from the passive incubation period to the active state seen in **Fig. 1** indicate that a critical coverage of Bi adsorbate on the Au surface triggers or initiates accelerated deposition. This is supported by electroanalytical and surface science measurements that show Au deposition on Au surfaces remains passive as the Bi adsorbate coverage, measured by X-ray photoelectron spectroscopy, builds, until a sharp acceleration of the Au deposition rate occurs beyond a threshold Bi coverage.² Initially, the actively growing deposit is non-uniformly distributed across the RDE surface⁴, similar to the localized behavior observed in many critical systems³⁴. For electrolyte of pH 9 the low current density of passive deposition is minimally affected by increasing adsorbate coverage until sharp acceleration of the current occurs once the coverage Γ_{Bi} , expressed as a fraction $\theta = \Gamma_{Bi}/\Gamma_{Bi,s}$ of the saturation coverage $\Gamma_{Bi,s}$ defined relative to the number of Au sites per area of deposit surface, reaches $\theta \approx 0.15$. Langmuir adsorption kinetics are assumed to describe the gradual process of Bi^{3+} accumulation as adsorbed Bi, with the local coverage θ increasing at a rate proportion to the concentration of the Bi^{3+} additive in the adjacent electrolyte (C_{Bi}) and fraction of available sites

$$\frac{d\theta}{dt} = k_+ C_{Bi} (1 - \theta) \dots \quad [2]$$

Terms accounting for mass conservation where the local surface area is changing (i.e., the CEAC mechanism) as well as removal of adsorbate by desorption into the electrolyte or incorporation

into the deposit are omitted for the time being. For given $Na_3Au(SO_3)_2$ and Na_2SO_3 concentrations, potential and pH, the rate constant k_+ is fixed and Eq. 2 can be integrated to obtain

$$\int_0^\theta \frac{d\theta}{1-\theta} = C_{Bi}k_+t \quad \xrightarrow{\text{yields}} \quad t = \frac{-\ln(1-\theta)}{k_+} \frac{1}{C_{Bi}} \quad [3]$$

whence the time t_{inc} to reach a critical fractional coverage for activation, θ_{crit} , is anticipated to depend linearly on $1/C_{Bi}$. Good agreement with such a dependence is observed for the incubation periods of the transients in **Fig. 1a-e** as summarized in **Fig. 1f**. The lower slope at more negative potential reflects increase of k_+ for reductive adsorption of Bi^{3+} with overpotential, which will be quantitatively parameterized below.

Several important limitations of the present construct are to be noted. Firstly, the y-axis intercepts of the fitted lines shift progressively from the origin as the potential is moved positive of -0.90 V. This deviation could arise from the absence of consumption and desorption terms in Eq. 2 and Eq. 3 that may play a significant role at more positive potentials¹⁻³. Indeed, there is clear indication of either, or both, in earlier multicycle voltammetric studies where the upper vertex potential was varied (Fig. 5 in Ref. 1). Likewise, there is a non-monotonic response of Bi^{3+} adsorption to hydrodynamics^{1,2} observed at -0.9 V (Fig. 3 in Ref. 1) and more positive potentials, albeit this is not necessarily at odds with simple Langmuir kinetics. With these caveats in place the dependence of k_+ as reflected in the variation of the incubation period on multiple system variables is quantified.

Rate Constant Dependencies

Measurements reveal the kinetic factor k_+ to be a function of the electrolyte composition, namely the $Na_3Au(SO_3)_2$ and Na_2SO_3 concentrations, and the applied potentials. The variation

of the incubation period as a function of $Na_3Au(SO_3)_2$ concentration with the other electrolyte components fixed is shown in **Fig. 2a**. Likewise, the effect of the Na_2SO_3 supporting electrolyte concentration with the other electrolyte components fixed is summarized in **Fig. 2b**. Logarithmic plots are used to enable simultaneous viewing of the widely differing values at the five different potentials examined in each electrolyte. In the first approximation the incubation period increases ten-fold with a ten-fold increase of the concentration C_{Au} of the metal ion, $Au(SO_3)_2^{3-}$, that equals the concentration of the $Na_3Au(SO_3)_2$ source. A similar dependence is observed with variation in the sulfite, SO_3^{2-} , concentration C_{SO_3} that equals the concentration of the Na_2SO_3 supporting electrolyte. Accordingly, proportional scaling of the incubation time with the concentrations of the constituents, $t_{inc} \propto C_{SO_3}C_{Au}$, is invoked for the concentration range examined. As $k_+ \propto t_{inc}^{-1}$, increasing electrolyte concentration is associated with slower adsorption, $k_+ \propto (C_{SO_3}C_{Au})^{-1}$, and a longer incubation period.

The impact of potential on the incubation period is captured implicitly in the preceding chronoamperometry and incubation period plots. The increasingly long duration of the incubation period on the RDE at more positive potentials, approximately a 100× increase over a +100 mV range for the electrolyte concentrations examined, is shown explicitly in **Fig. 3**. The slowing of Bi^{3+} adsorption with increasing $Au(SO_3)_2^{3-}$ concentrations, just noted, is captured implicitly this figure.

Expressed as a potential activated process the incubation time can be fit to

$$t_{inc} \propto e^{\alpha_{Bi}nFV/RT} \propto e^{V/\Delta V_0} \quad [4]$$

with the data for the lower Au concentrations reasonably well represented by $\alpha_{Bi} = 0.4$, with $n = 3$ for reduction of the triply ionized Bi^{3+} , $F = 96485 \text{ C}\cdot\text{mol}^{-1}$, $R = 8.314 \text{ J}\cdot\text{mol}^{-1}\cdot\text{K}^{-1}$ and $T = 293$

K. This is equivalently expressed using $\Delta V_o \approx 0.02$ V, i.e., the incubation period increases $\approx 2.7 \times$ (i.e., e^1) every +20 mV. The potential dependence is consistent with reductive adsorption of Bi^{3+} to Bi. That said, it is noted that the modest charge transfer kinetics and dilute concentration of the Bi^{3+} are such that its electroadsorption makes a small contribution to the overall charge balance compared to that for the reduction of $Au(SO_3)_2^{3-}$, and thus the charge associated with Bi^{3+} adsorption is not tracked in the following analysis. For the purposes of subsequent modeling, the above dependencies are all assumed to extend and be applicable to the more positive potentials used for experimental filling of the deepest and highest aspect ratio features, e.g., -0.72 V.

Subject to the assumption that $k_+ \propto t_{inc}^{-1}$, the effects of the gold salt and supporting electrolyte concentrations and the potential are combined to give a generalized constitutive expression for the Bi^{3+} adsorption rate constant k_+

$$k_+ = k_+^0 \frac{C_{Au}^{Ref} C_{SO_3}^{Ref}}{C_{Au} C_{SO_3}} e^{-(V - V_{Ref})/\Delta V_o} \quad [5]$$

The inverse dependencies on metal ion and sulfite concentrations as well as the exponential dependence on potential have been scaled to reference conditions associated with void-free, bottom-up filling of high aspect ratio trenches: $C_{SO_3}^{Ref} = 0.64$ mol·L⁻¹, $C_{Au}^{Ref} = 0.16$ mol·L⁻¹ and $V_{Ref} = -0.72$ V. This leaves only the constant k_+^0 , having the same units as the full kinetic factor k_+ , as a fitting parameter.

Beyond the adsorption process, tracking the evolution of Bi coverage during growth requires consideration of a series of other terms. Of primary importance to bottom-up feature filling is the impact of surface area change that accompanies growth. Surfactant conservation is captured by the curvature enhanced adsorbate coverage (CEAC) formalism where the rate of local change in

coverage due to changing area, $d\theta/dt$, is the product of the existing coverage θ , normal interface velocity v (i.e., deposition rate), and local curvature κ , with the latter being positive for concave and negative for convex segments. Likewise, a complete thermodynamically correct description of adsorbate evolution requires a reversible process for additive loss by desorption, not to mention reversible or irreversible loss by additive consumption into the growing solid, with some combination thereof being necessary for steady-state alloy composition and additive coverage to be attained. Such removal of adsorbed Bi is understood to be significant in this system given the observed self-passivation of the activated surfaces following bottom-up feature filling.¹⁻⁸ Many prior growth models have detailed metal deposition-derived consumption or burial of additives. For suppressed systems where the surface is practically saturated with a blocking inhibitor, disruptive consumption is captured as the product of the suppressor coverage and the growth velocity scaled by a rate constant scaling factor for the adsorbate burial k_{bur} .^{34-36,38} The rate constant has units of inverse-length that reflect the growth distance over which exponential decay by burial would reduce an initial coverage by e^{-1} . In contrast, for accelerated systems where functionality derives from a more dilute lattice gas species, the consumption process can be coverage dependent. In particular, consumption may be associated with the accelerator species interacting with one another such that the process is higher order, e.g. quadratic, in the surfactant coverage.⁴⁴ Occurring in parallel with deactivation by incorporation, the reversible process of additive desorption back into the electrolyte includes a rate constant scaling factor k_{des} that has units of inverse-time and reflects the period over which the adsorbate coverage in excess of the steady state value decreases by e^{-1} . Finally, any local enrichment of Bi coverage is also subject to the countering action of diffusion along the surface. Combining the above terms the full expression for Bi adsorbate evolution in the Bi-Au system takes the form:

$$\frac{d\theta}{dt} = \kappa v \theta + \left[k_+^0 \frac{C_{Au}^{Ref} C_{SO_3}^{Ref}}{C_{Au} C_{SO_3}} e^{-(V-V_{Ref})/\Delta V_o} \right] C_{Bi}(1-\theta) - k_{bur} v \theta^2 - k_{des} \theta + D_{s,Bi} \nabla_t^2 \theta \quad [6]$$

Inclusion of the area change adsorbate conservation term is supported by images of Au bottom up filling shown in **Fig. 4** for trenches and electrolytes such as those detailed previously.¹⁻⁷ Active deposition originates at the lower corners of features followed by sustained extreme bottom-up filling in a manner consistent with CEAC-based superconformal deposition.

The effectiveness of the Bi layer in lifting the sulfite suppression of the $Au(SO_3)_2^{-3}$ and remaining segregated on the growing interface are questions worthy of further study. In terms of solid state properties, the binary phase diagram for the Au-Bi system indicates very limited solid solubility of Bi in crystalline Au with a maximum of only 0.06 at. % at approximately 900 °C, and a solubility lower than 0.001 at. % at 500 °C with further decrease expected toward room temperature.⁴⁶ Even at the intermediate temperature, for Au deposition on a (111) oriented crystalline Au with spacing of 0.22 nm between the (111) planes, a value of $k_{bur} = 0.00001/0.22 \text{ nm}^{-1}$ ($0.045 \text{ } \mu\text{m}^{-1}$) is obtained for the reciprocal of the length scale over which the coverage on a Bi-saturated surface could be incorporated subject to the solubility threshold in the solid. Burial subject to the constraint of equilibrium solubility occurring at a length scale of $\approx 20 \text{ } \mu\text{m}$ is not likely to significantly impact feature filling at the feature length scales of interest. On the other hand, despite the immiscible nature of the bulk alloy system, surface alloy formation is widely known to occur in coinage metal (Au, Ag, Cu, Sn) - heavy metal (Tl, Pb, Bi) systems.⁴⁷ Indeed, Bi is known to electroadsorb and form a variety of ordered under potential deposited (upd) overlayers on the different low index Au surfaces.⁴⁸⁻⁵³ Accordingly, consumption of adsorbed Bi by burial in the growing deposit is taken to be a higher order process in its coverage subject to Bi-Bi interactions. This motivates the quadratic dependence on Bi coverage of the consumption term in

Eq. 6 that is further scaled with the metal deposition rate so that the prefactor also has units of inverse length. While the relatively high value of $k_{bur} = 10 \mu\text{m}^{-1}$ specified in Table I suggests a seemingly small $\approx 0.1 \mu\text{m}$ length scale for burial, due to the quadratic dependence on coverage it actually is consistent with good surfactant quality at low coverages.

The final term in Eq. 6 accounts for diffusion along the surface of the Au deposit with surface diffusivity $D_{s,Bi}$ acting upon gradients of surface coverage. The well defined, sharp corners in bottom-up Au filling features suggest that this term is not a key factor in the filling evolution in electrolytes of pH below 10. Nonetheless, its inclusion and related smoothing of the adsorbate distribution also help stabilize the numerical code used to obtain the simulations. The diffusion coefficient of $1 \times 10^{-12} \text{cm}^2\cdot\text{s}^{-1}$ in Table I is a plausible estimate based on values reported for Bi surface diffusion on Cu surfaces near room temperature, although it should also be noted that significant variations with coverage and phase structure are observed.^{54,55} That said, in the simulations that follow this term has only a modest impact after bottom-up filling initiates.

Before proceeding further, it is noted that previously published¹ images of bottom-up filling in the shallowest of trenches exhibit essentially uniform activation across the trench bottoms that contrasts with the CEAC-based initiation discussed above. However, the results of deposition in the same size trenches shown in **Fig. 4c** and **Fig. 4d**, particularly those in the latter for filling in trenches with a freshly deposited Au seed layer, suggest some unintentional aspect of the original Au seed layer on the non-silicon dielectric matrix unique to these specimens might be responsible for the difference. Aside from the initial nucleation process, the subsequent growth geometry and bottom-up Au filling evolution in a wide variety of deeper trenches and vias appears to be independent of seed layer (e.g., Pt or Au).²⁻⁷

Strategy for Parameter Determination

An estimate for the upper bound of the ratio k_+^0/k_{des} in Eq. 6. can be obtained from demanding passivation of the free-surface occur at potentials and conditions used for bottom-up feature filling, consistent with experimental observation. In particular, an estimate of the upper bound for the ratio k_+^0/k_{des} can be obtained by ignoring burial and imposing steady state, $\frac{d\theta}{dt} = 0$, for the planar surface (i.e., $\kappa = 0$) with uniform coverage (i.e., $\nabla_t^2\theta = 0$) in Eq. 6 for bulk electrolyte concentrations and a steady state value for the coverage θ low enough at the applied potential that deposition on the planar surface occurs at the slower passive rate. Considering only the adsorption and desorption terms in Eq. 6, for the reference electrolyte concentrations and potential and other parameters in Table I, the ratio k_+^0/k_{des} is high enough to achieve steady state coverage $\theta = 0.13$ on the field. Considering only the adsorption and burial terms with the same parameters, and using the deposition rate versus coverage relationship to be detailed later, the ratio k_+^0/k_{bur} is barely sufficient to maintain steady state coverage of approximately 0.11. With concurrent desorption and burial, the steady state coverage on the field is somewhat less than the lower value. One might consider adjusting such analysis to account for the gradient across the boundary layer and the impact of the burial term under the same conditions, and a particular steady state coverage θ might be selected to yield passivation consistent with experimental observations of the depth at which passivation occurs under particular conditions of transport (i.e., boundary layer thickness) and potential. However, for the purposes of developing a general mechanistic understanding, the above simple analysis is sufficient. The value of the rate constant k_+^0 was selected to capture the duration of the incubation period and obtain consistency of feature filling predictions with the experimental void-free filling of 60 μm deep trenches of aspect ratio 60 observed in electrolyte of the reference

composition at the reference potential of -0.72 V.⁶ The coefficient for the burial term is large enough to prevent Bi coverage on the bottom surface during active bottom-up filling from exceeding several tenths of a monolayer.

Trench Filling Computational Model

Finite element method (FEM) computations are used to simulate Au electrodeposition in trenches having specified W and depth H at a pitch P as shown schematically in **Fig. 5**. The two-dimensional (2D) model simulates Au deposition with a fixed boundary layer over the filling feature through which ion transport occurs by diffusion and electromigration; the impact of convection is accounted for only by the thickness of the boundary layer that is related by the Levich equation to the substrate rotation rate. The reference electrode and counter electrode are combined in a common plane located at a distance L_{RE} above the boundary layer δ . The electric potential is set equal to zero at the reference/counter electrode. The concentrations of the major species (Na^+ , $Au(SO_3)_2^{3-}$, SO_3^{2-} and Bi^{3+}) are set equal to the concentrations of the bulk solution (C_i^o) at the top of the boundary layer based on full disassociation of the electrolyte constituents and the nominal additive concentration.

The boundary conditions correspond to filling of an array of trenches that is periodic in the x -direction at pitch P consistent with the gratings typically filled using this process. The concentration C_i and flux \vec{N}_i of each species in the electrolyte domain are related by the Nernst-Planck equation,

$$\frac{dC_i}{dt} = -\nabla \cdot \vec{N}_i = -\nabla \cdot (-z_i u_{m,i} F C_i \nabla \phi - D_i \nabla C_i) \quad [7]$$

including diffusion and migration but excluding convection as noted earlier. The other terms have their usual identities: the species' charge z_i , diffusion coefficient D_i , Faraday's constant F , and mobility $u_{m,i}$ calculated by the Einstein relationship

$$u_{m,i} = \frac{D_i}{RT} \quad . \quad [8]$$

The combined concentrations of $Na_3Au(SO_3)_2$ and Na_2SO_3 are high enough that the potential in the electrolyte (ϕ) is well approximated by Laplace's equation

$$\nabla^2 \phi = 0 \quad , \quad [9]$$

which neglects potential variation in solution arising from ionic gradients. The current density \vec{j} associated with the $Au(SO_3)_2^{3-}$ flux through the electrolyte is given by Ohm's law

$$\vec{j} = -\kappa \nabla \phi \quad [10]$$

with the conductivity of the electrolyte κ . Consistent with the periodicity of the trench array, a zero flux symmetry condition is imposed at both sides of the cell ($x = \pm P/2$) for gradients of solution potential

$$\frac{\partial \phi}{\partial x} = 0 \quad [11]$$

and zero flux conditions for the species' concentrations in solution are imposed at the same locations

$$\frac{\partial C_i}{\partial x} = 0 \quad . \quad [12]$$

Net accumulation of Bi adsorbate on the electrode from the electrolyte follows Eq. 6, with activation of Au deposition being a function of Bi accumulation from the electrolyte subject to its

incorporation into the growing deposit and/or desorption into the electrolyte and surface diffusion. The current density is translated into growth velocity, v , using Faraday's constant, the net ionic charge of the reaction $n = 1$ and the molar volume Ω of solid Au

$$v(\theta, C_{Au}, \eta) = \frac{\Omega}{nF} \frac{C_{Au}}{C_{Au}^o} j_{\eta}(\eta, \theta) \quad [13]$$

A linear dependence on the local metal ion concentration C_{Au} has been assumed. The Au deposition rate also depends on the overpotential η at the interface. The one electron reduction of $Au(SO_3)_2^{-3}$ to the metallic $Au(0)$ on the workpiece releases the two SO_3^{2-} ligands into the adjacent electrolyte as free anions.

The most unique aspect of the Bi-accelerated Au deposition is the nonlinear transition between the passive and active deposition states. The transition is centered on a nonzero or critical Bi coverage, θ_{crit} , consistent with these experimental observations. Accordingly, for modeling, the rate of Au deposition is taken to be a nonlinear function of the Bi accelerator coverage θ . The potential-dependent Au deposition rate is herein expressed with current density $j(\eta, \theta)$ being a hyperbolic tangent function of the Bi coverage θ

$$j(\eta, \theta) = \frac{1}{2} \left[(j_1(\eta) + j_0(\eta)) + (j_1(\eta) - j_0(\eta)) \tanh \left(\frac{\theta - \theta_{crit}}{\Delta\theta} \right) \right] \quad [14]$$

chosen simply to give a defined transition between the current densities for fully passive $j_0(\eta)$ and active $j_1(\eta)$ surfaces, each of these depending on overpotential in accord with voltametric measurements of the two limiting cases. In this formulation the transition occurs principally over a range of Bi coverages centered around the critical value θ_{crit} as reflected in the observed incubation period already detailed. More than 76 % of the change of the Au growth rate occurs over a coverage range $2\Delta\theta$, while 96 % of the change occurs over a coverage range $4\Delta\theta$. For the

values in Table I, activation at adsorbate coverages near $\theta_{crit} = 0.15$ is not especially sharp, occurring over the range $4\Delta\theta = 0.08$ that is slightly more than one-half the nominal value for activation. The sharpness of the transition, or more appropriately the relative lack thereof, is not the determining element in the behavior observed in the simulations. Rather, it is the absence of significant activation over a range of lower coverage values, well supported experimentally, that is a key component of the mechanism. Use of the smoothly varying $\tanh()$ form facilitates numerical convergence that a truly critical system construct would otherwise hamper.

A Butler-Volmer dependence on overpotential η at the working electrode is used to describe the current densities in the passive $j_0(\eta)$ and active $j_1(\eta)$ states

$$j_{0,1}(\eta) = j_{0,1}^o \left(e^{\frac{-\alpha_{0,1}F}{RT}\eta} - e^{\frac{(1-\alpha_{0,1})F}{RT}\eta} \right) \quad [15]$$

although the overpotentials examined are large enough that the back reaction term is negligible.

The applied potential V_{app} is related to the overpotential through

$$V_{app} = \eta + \phi + E_{rev} \quad [16]$$

where the potential ϕ within the electrolyte, evaluated at the electrolyte/deposit interface, captures the potential drop associated with dissipative ohmic losses between the workpiece (substrate) and the reference electrode due to current flow through the electrolyte. The distance to the simulated reference electrode position is congruent with the experimental geometry. The overpotential driving electrodeposition is referenced somewhat arbitrarily to $E_{rev} = -0.4$ V (vs SSE), rather than evaluated from open circuit potential, and considered independent of the metal ion concentration at the electrolyte/deposit interface as the process is not reversible (dissolution is strongly inhibited). The charge transfer coefficient $\alpha_1 = 0.5$ for the active state in Table I was obtained from

the slope of return scans in cyclic voltammetry plotted on logarithmic scale; a potential dependence of some (130 to 150) mV per decade of current density, which is reasonably consistent with that used for the active state here, has been noted at elevated current densities in a different gold sulfite electrolyte.³³ The corresponding value $\alpha_0 = 0.2$ for the passive state was obtained from the negative-going scans.^{1,7}

The passive exchange current density j_0^o is set to yield a passive sidewall growth rate somewhat faster than $0.01 \mu\text{m}\cdot\text{h}^{-1}$ to be consistent with observed sidewall deposition rates for partially filled trenches in $0.08 \text{ mol}\cdot\text{L}^{-1} \text{ Na}_3\text{Au}(\text{SO}_3)_2$ concentration electrolytes⁵ at -0.72 V as well as upper sidewall deposit thickness in filled $60 \mu\text{m}$ deep $1 \mu\text{m}$ wide trenches⁶ in the $0.16 \text{ mol}\cdot\text{L}^{-1} \text{ Na}_3\text{Au}(\text{SO}_3)_2$ concentration electrolyte that are being modeled at the same potential. The active exchange current density j_1^o is set to yield a period of active bottom-up filling of the $60 \mu\text{m}$ deep trenches consistent with the approximately 6 h period of active bottom-up deposition during experimental filling (i.e., an active deposition rate of approximately $10 \mu\text{m}\cdot\text{h}^{-1}$).⁶ The dynamic range between the fully active and passive deposition rates is thus nearly 1000. The passive and active current densities in previously published voltammetry indicate passive and active deposition rates at -0.72 V of approximately $0.01 \text{ mA}\cdot\text{cm}^{-2}$ and $1.0 \text{ mA}\cdot\text{cm}^{-2}$, respectively, giving a dynamic range of 100.⁷ The passive rate used here is lower than the voltametric value by roughly a factor of three while the active rate used here is higher than the voltametric value by a similar factor of three. Reduction of the passive current density accounts for possible parasitic contributions in the voltammetry already noted; the measured current density overestimates the current density associated with the passive metal deposition. Increase of the active current density from that in the voltammetry derives from localization of deposition on the planar surface RDE surface that is

characteristic of deposition in this electrolyte-additive system¹ at the more positive potentials; current densities estimated using the full area of the RDE underestimate the local current density actually associated with regions of active deposition on the RDE surface.

The $Au(SO_3)_2^{3-}$ flux from the electrolyte to the electrode interface (outward surface normal \hat{n}) is essentially equal to the local current density $j(\eta, \theta)$ at the electrode

$$-(z_{Au}u_{m,Au}FC_{Au}\nabla\phi + D_{Au}\nabla C_{Au}) \cdot \hat{n} = \frac{1}{nF}j(\eta, \theta) \quad [17]$$

with the net charge of the reaction $n = 1$. The charge transfer reaction associated with reduction of dilute Bi^{3+} upon adsorption is neglected in the simulations as it would not contribute significantly to the overall currents. The normal flux of Bi^{3+} in the electrolyte to the interface is equated to the net rate of its adsorption and desorption yielding evolution from the initial coverage of zero according to

$$-(z_{Bi}u_{m,Bi}FC_{Bi}\nabla\phi + D_{Bi}\nabla C_{Bi}) \cdot \hat{n} = \Gamma_{Bi,s}(k_+C_{Bi}(1 - \theta) - k_{des}\theta) \quad [18]$$

with saturation coverage values, $\Gamma_{Bi,s}$, equated to the site density on the Au (111) surface. Finally, the flux of free sulfite released to the electrolyte at the interface by the reduction of the $Au(SO_3)_2^{3-}$ complex ions to Au deposit yields

$$-(z_{SO_3}u_{m,SO_3}FC_{SO_3}\nabla\phi + D_{SO_3}\nabla C_{SO_3}) \cdot \hat{n} = -2\frac{1}{nF}j(\eta, \theta) \quad [19]$$

The full system of equations is solved numerically in 2D using a finite element method employed in the COMSOL Multiphysics version 5.5 software package and the default solver, implementing the following modules: tertiary current distribution, separate coefficient form boundary partial differential equations for Bi and Au, and deformed geometry. A finer 2D triangular mesh was

selected for the lower region and upper region of the trench, including an even finer mesh along the edges of these regions, with a coarse mesh to model the essentially 1D flow of charge between the top of the boundary layer and the reference electrode. Automatic remeshing was enabled. Even with surface diffusion, moving boundary smoothing was required to accommodate the mathematical stiffness of the simulations caused by the high ratio of the active and passive current densities and highly localized nature of adsorbate buildup through the CEAC mechanism during active bottom-up filling where the lower surface abuts the sidewalls.

Trench Filling Simulations

Simulations are generated for Au filling of trenches under potentiostatic conditions in $0.16 \text{ mol}\cdot\text{L}^{-1} \text{Na}_3\text{Au}(\text{SO}_3)_2 + 0.64 \text{ mol}\cdot\text{L}^{-1} \text{Na}_2\text{SO}_3$ electrolyte containing $50 \text{ }\mu\text{mol}\cdot\text{L}^{-1} \text{Bi}^{3+}$, for which experimental filling has been detailed in features having a number of different depths and aspect ratios. The kinetic parameters and other constants are summarized in Table I. Simulations capturing the growth front position during bottom-up Au filling at -0.72 V of $1 \text{ }\mu\text{m}$ wide, $2 \text{ }\mu\text{m}$ pitch trenches having three different depths are shown in **Fig. 6**. The predicted deposition contours capture the predicted bottom-up filling, and the indicated deposition times make clear the substantial, albeit differing, incubation periods for the different depth features. In all three cases deposition is initially passive and conformal, with accelerated deposition initiating from the lower corners and then proceeding upward from the bottom surface toward the opening of the trench.

The underlying interplay between chemistry, adsorption kinetics and the CEAC mechanism through the evolving surface area is captured as a function of time for the particular case of filling in the $20 \text{ }\mu\text{m}$ deep trench in **Fig. 7**; the results are qualitatively representative of all three cases. The timescale and deposition and adsorption rates are such that only modest depletion of both

metal ion and Bi^{3+} down the trenches is associated with the filling evolution; the simulations are thereby consistent with the uniformly thick passive deposits observed experimentally on the sidewalls prior to the transition to bottom-up filling. The gradient of Bi adsorption kinetics, a fractional difference of $< 1\%$ between field and trench bottom given the modest gradient of $Au(SO_3)_2^{3-}$ (and offsetting SO_3^{2-}) concentration, yields only a similarly modest enhancement of coverage on the lower surface by 10000 s. Subsequent enhancement of Bi coverage by the CEAC mechanism results in significant acceleration (i.e., coverage exceeding $\theta_{crit} - 2\Delta\theta$ for the growth rate - coverage dependence defined by Eq. 14). The bottom-up filling manifests adsorbate accumulation on the active surface through the CEAC mechanism that is sufficient to counter adsorbate burial and decreasing adsorption kinetics as filling progresses toward the trench opening. Of the constituent components, fractional depletion of the $Au(SO_3)_2^{3-}$ concentration is seen in **Fig. 7** to be the most substantial at the start of active bottom-up filling, its concentration returning to near bulk value as filling progresses and the bottom surface comes closer to the field. Rejection of SO_3^{2-} during the Au deposition mirrors this response, an increase rather than a decrease, but fractionally smaller given the higher bulk SO_3^{2-} concentration in the electrolyte. A slight increase of the Bi^{3+} concentration as filling progresses reflects additive desorption from the surface where area loss brings the local coverage (through the CEAC mechanism) to a value that exceeds the Langmuir equilibrium coverage. Significantly, as bottom-up filling brings the active surface to electrolyte approaching bulk concentrations, both the Bi^{3+} adsorption kinetics on the active surface and the steady state adsorbate coverage on the sidewalls being incorporated through the CEAC mechanism decrease. At approximately 26000 s positive feedback between slowing deposition rate from decreasing adsorbate coverage and slowing accretion of adsorbate from eliminated sidewall area through the CEAC mechanism, given the slowing deposition rate, results

in sudden deactivation evident especially in the deposition current and adsorbate coverage transients in **Fig. 7**. Deposition, which has fully filled the trench by 27000 s, thereby remains constrained to the trench through the end of the simulation at 50000 s in **Fig. 6**.

Considering the details of the transients in **Fig. 7** in more detail, Bi^{3+} is essentially at the bulk concentration within the trench throughout the filling process, with depletion at the trench bottom not exceeding the 0.3 % predicted at the start of adsorption on the Bi-free surface. Thus, albeit the coverage does initially increase slightly faster on the field, given the miniscule gradient, adsorbate coverage on the field and bottom surfaces differs minimally through the first 10000 s. The approach to steady state Bi coverage, evident in the asymptotic trend on the field, steadily eliminates even the small gradient of the Bi^{3+} concentration and the value at the trench bottom returns to the bulk value. Early reduction of the Bi^{3+} concentration gradient allows the contrary impact of the increasing $Au(SO_3)_2^{3-}$ gradient to dominate the Bi^{3+} adsorption kinetics, such that the coverage on the bottom exceeds that on the field after 2000 s. The gradually increasing Bi coverage and, thereby, deposition current is associated with only ≈ 1.5 % depletion of the metal ion concentration (i.e., to 98.5 % of bulk value) at the bottom of the trench. However, further increase of the adsorbate coverage through the CEAC mechanism brings the Bi coverage at the bottom to an average value of ≈ 0.11 by 15000 s and ≈ 0.13 by 16500 s, values $2\Delta\theta$ and $\Delta\theta$ below $\theta_{crit} = 0.15$, as/and deposition accelerates. The positive-feedback loop of increasing adsorbate coverage at the trench bottom (through both the CEAC mechanism and accelerating Bi^{3+} adsorption kinetics given decreasing $Au(SO_3)_2^{3-}$) and accelerating bottom-up filling (through the increasing adsorbate coverage) yields a rapid, nonlinear activation that is manifest in all the simulated variables. The concurrent enhancement of adsorption kinetics associated with further depletion of the $Au(SO_3)_2^{3-}$ concentration at the trench bottom, from 1.5 % to 6 % as bottom-up

filling driven by the CEAC mechanism commences, further stabilizes active deposition at the bottom. Activation occurs rapidly once it begins despite the relatively broad coverage range associated with full activation in Eq. 14 (i.e., $4\Delta\theta = 0.8$ is more than one-half of $\theta_{crit} = 0.15$) in great part because of the nearly thousand-fold acceleration that activation provides.

Significantly, while the bottom surface is accelerating, the asymptotic approach to steady state coverage of ≈ 0.1 monolayers on the planar field (note the steady-state value after filling is completed at 40000 s defined by adsorption balancing desorption and burial absent both gradient and CEAC amplification) keeps deposition on the field and higher in the trench in the passive state. It is the existence of a range of adsorbate coverage θ yielding passive deposition, i.e., between zero and $\theta_{crit} - 2\Delta\theta$ for the formulation in Eq. 14, and steady state coverage falling in this range that enables active deposition to remain localized toward the bottom surface.

There is an additional important impact of the fact that the adsorption, desorption and burial kinetics used in these simulations yield steady-state coverage of Bi adsorbate on the field below that required for significant acceleration. This sub-critical steady-state coverage, through the loss of the gradient-derived differential that necessarily accompanies filling, underlies deactivation of the upward moving active surface as it approaches the field. The $Au(SO_3)_2^{3-}$ concentration differential, in conjunction with the nonlinear coverage-deposition rate relationship, thus not only facilitates the nonlinear CEAC-derived activation and filling but, through its elimination during filling, also underlies the self-passivation that follows.

In addition to capturing the localization, bottom-up filling and passivation observed experimentally, the simulations in **Fig. 6** anticipate inception at the lower corners observed experimentally in **Fig. 4**; initial acceleration in the concave corners of features is a ubiquitous

prediction of CEAC-based models. That said, there are differences between the details of simulation and experiment that presumably reflect deviation of the model as formulated or inaccuracy in the kinetics used for the modeling. Flat bottoms are seen in most specimens filled in the pH 9.0 electrolytes while the simulations exhibit a curved profile throughout the duration of filling; the predicted curvature depends on parameters including the surface diffusion coefficient and burial and desorption kinetics. Interestingly, analogous curvature is observed in trenches filled in pH 10.3 electrolytes⁴. The simulated current transient during the period of bottom-up filling also exhibits a gradual decline whereas experimental filling exhibits a gradual further increase of current after the initiation of bottom-up filling. The change in the simulated current is consistent with the initial contribution of passive deposition on the sidewalls; the gradual decrease thus reflects the reduction of sidewall area, while the final sharp drop to near zero is associated with passivation of the active area within the filled trench. The rising current observed experimentally, particularly in the deepest trenches⁷, on the other hand, suggests the impact of increasing $Au(SO_3)_2^{3-}$ concentration as filling progresses. The impact of transport will be returned to later.

The acceleration of deposition within the trench is accompanied by a maximum 16 mV potential drop across the electrolyte from the reference electrode to the field of the substrate, with minimal drop within the trench itself; the potential drop scales with the current density defined by the planar area of the patterned substrate at 20 mV per $-1 \text{ mA}\cdot\text{cm}^{-2}$ for the cell geometry and electrolyte resistivity used here (or, equivalently, per $-20 \text{ }\mu\text{A}\cdot\text{m}^{-1}$ current per length of trench for 2 μm trench pitch). The magnitude of this ohmic term is controlled by the active deposition rate, pattern geometry, and system resistance among other factors. The ohmic reduction of overpotential decreases the deposition rate (Eq. 15) and the adsorption kinetics (Eq. 6). It thereby decreases the

steady state adsorbate coverage on the field and upper regions of the trench while increasing the filling time. Larger ohmic losses can also change the nature of the filling evolution.

Simulation of filling in 60 μm deep trenches yields analogous results (**Fig. 8**). As with the shallower trenches, superconformal deposition begins within the trench as the net impact of $\text{Au}(\text{SO}_3)_2^{3-}$ and SO_3^{2-} concentration gradients on the kinetics of Bi adsorption at the bottom of the feature more than compensate for the impact of the decreased Bi^{3+} concentration itself. Area reduction at the trench bottom again accentuates the impact of this differential on the local accelerator coverage through the CEAC mechanism, thereby driving the local coverage up to values consistent with active deposition as per Eq. 14. Following its initiation, bottom-up filling is maintained by the passivation of sidewalls and field with void-free filling again tied to steady-state coverages of the Bi adsorbate below that yielding significantly activated deposition. Further acceleration of the active deposition rate as the growth front rises toward the field is manifest in the progressive increase of spacing between contours 6 through 10, a variation also evident with the 50 μm deep trenches in **Fig. 6**. Depletion of the $\text{Au}(\text{SO}_3)_2^{3-}$ reaches 18 % when bottom-up filling commences, significantly greater than that predicted for filling of the 20 μm deep trenches in **Fig. 6** as a result of the longer distance for transport. The increased, but still limited, depletion is still indicative of kinetic rather than transport control. Higher Bi coverage during filling of the taller trench reflects principally the balance of CEAC enhancement with burial and desorption across the narrower active surface resulting from thicker passive sidewall deposits after longer deposition time; there is less area on the bottom-up growth front onto which the Bi collected from the sidewalls can be distributed and higher steady state coverage required for desorption and burial to balance that accumulation. Experimental results (Fig. 15 in Ref. 6) exhibit both a smoother rise upon activation and smoother decline during passivation. Determining how much these differences

reflect averaging across experimental substrates versus, for example, a different growth rate versus coverage dependence than that assumed in Eq. 14 and/or differences in other parameters will require deeper study.

A consistent trend in filling with the applied potential has been noted in features of widely differing aspect ratio for the Bi^{3+} -activated gold sulfite electrolytes. As the potential is decreased to more negative values a transition from conformal filling with seam formation to the desired bottom-up superconformal filling is observed.^{1-3,6} At still more negative potentials, reduced bottom-up filling (truncated bottom-up filling) with progressively larger trapped voids is observed¹⁻⁷. The predicted transition of filling geometry with applied potential is shown in **Fig. 9** for the same array of 60 μm deep and 1 μm wide trenches, based on the kinetics in Table I. Bottom-up filling is predicted at -0.72 V as well as -0.74 V, consistent with experiment in trenches of these dimensions and electrolyte of this composition for which bottom-up filling is seen at the same potentials in **Fig. 10**. Bottom-up filling followed by void-formation through sidewall impingement (truncated bottom-up filling) is predicted at more negative potentials of -0.78 V and -0.76 V, albeit only marginally in the latter case, consistent with experimental failure to fully fill at -0.76 V. Higher magnification insets capture the seamlike voided regions in the simulations. The increased passive deposition at these more negative potentials as per Eq. 6 yields thick conformal deposits on the sidewalls during the course of filling. As a result, the void caused by impingement of the sidewall deposits that halts both simulation and bottom-up filling at -0.78 V is seamlike. An analogous seam with an extremely small void located at the bottom is obtained at -0.76 V. The narrowness of the seams manifests substantial depletion of the $Au(SO_3)_2^{3-}$ concentration only after significant thickening of the sidewall deposits. Broadening of the void toward the bottom of the

trench at -0.78 V yields the classic reactant-depletion derived keyhole shape, albeit the seam is narrow in the high aspect ratio trench.

Formation of a seam-like void is also predicted at the most positive potential examined, -0.70 V, but in this case with uniformly slow and conformal passive deposition. In the absence of significant reactant depletion or bottom-up filling the resulting center-line seam extends from a distance of one-half the trench width W from the trench bottom all the way to the surface. This result is consistent with broader experimental observation of conformal filling at potentials positive of those yielding bottom-up filling; there are no directly corresponding experimental results for trenches of this particular size. Even with assistance from the CEAC mechanism, at such positive potential the potential- and concentration gradient-defined kinetics are insufficient, countered as they are by burial and especially desorption, to raise the Bi coverage at the trench bottom high enough for accelerated bottom-up filling to occur. The simulations in **Fig. 9** thus capture the experimentally observed potential-dependent transition from void-free bottom-up fill to voided fill shown in **Fig. 10** as applied potential is made more negative as well as the transition to conformal fill observed more broadly as potential is made more positive.

The simulations also capture finer details seen in other experiment, including decreasing thickness of the deposits on the sidewalls at more positive potentials just prior to or after termination of bottom-up filling. However, experiment and simulation differ in other details. The simulations in **Fig. 9** overestimate the fill height associated with self-passivation in **Fig. 10**, perhaps reflecting failure to account for splay below the openings of experimental features, which would accelerate re-passivation by diluting adsorbate coverage. The incubation period before bottom-up filling at -0.74 V is also less than one-third that predicted for -0.72 V, reflecting the potential dependent kinetics of the Bi^{3+} adsorption and the metal deposition. This is a far more

substantial change than the decrease from 47000 s to 37000 s seen in the experimental result. Likewise, the activation and passivation of bottom-up filling yield a steeper rise and fall in the current transients than is observed in the experiment. Voiding with predicted truncated bottom-up filling at -0.76 V, and even at -0.78 V, is also far narrower than the actual occluded voids at -0.76 V (see also higher magnification in Fig. 14 of Ref. 6), and experimental observation of truncated bottom-up deposition more broadly exhibits wider voids.

Focusing on this last difference in particular, modest depletion of the $Au(SO_3)_2^{3-}$ metal ion nearly until failure in both simulations underlies the thick and uniform deposition along the height of the sidewalls. Strongly subconformal filling is also avoided in great part by ohmic losses, mirroring the current transients also included in **Fig. 9**, that reduce the deposition rates, passive and active. The potential drop is predicted to exceed 60 mV (again at 20 mV per $1 \text{ mA}\cdot\text{cm}^{-2}$) for deposition at -0.78 V, although the peak current of $\approx -3 \text{ mA}\cdot\text{cm}^{-2}$ is likely unrealistically high given that the maximum of $\approx -2.2 \text{ mA}\cdot\text{cm}^{-2}$ in the simulation at -0.76 V exceeds that of the corresponding experimental transient by a multiple of nearly 3. The wider voids in the truncated bottom-up filling of experiment in **Fig. 10** suggest larger gradients of the $Au(SO_3)_2^{3-}$ concentration in the un-narrowed trench yielding faster activation of the bottom surface in conjunction with slower passive deposition.

A simulation of truncated bottom-up filling with parameters modified to achieve such conditions is shown in **Fig. 11**. The diffusion coefficient for the metal ion D_{Au} has been decreased from $5 \times 10^{-6} \text{ cm}^2\cdot\text{s}^{-1}$ to $1 \times 10^{-6} \text{ cm}^2\cdot\text{s}^{-1}$ to increase the gradient of $Au(SO_3)_2^{3-}$ concentration associated with active deposition. The simulation has been conducted at the more positive potential of -0.72 V to reduce the passive deposition rate in lieu of changing kinetic parameters. An

additional change has been made to the electrolyte conductivity κ , which has been increased from $10 \text{ S}\cdot\text{m}^{-1}$ to $20 \text{ S}\cdot\text{m}^{-1}$ to reduce the resistive losses that could restrict active area and localize deposition toward the bottoms of recessed features as in suppressor-containing electrolytes³⁴⁻³⁹. Deposition contours colored according to the predicted Bi coverage capture the evolution of filling from 0 s to 21000 s in 3000 s increments. The contours from 12000 s to 21000 s in the lower half of the trench are shown separately colored according to the metal deposition rate. The truncated bottom-up fill exhibits a visibly wider voided region than the simulations in **Fig. 9** that is more consistent with the experimental truncated bottom-up filling in **Fig. 10** as well as published images for a variety of features.

Closer examination of the contours reveals activation at the corners at 12000 s with full activation of the bottom surface and bottom-up filling clear by 15000 s but then halted by 18000 s concurrent with activation of deposition on the sidewalls. Near-zero metal ion concentration at the bottom caused by deposition along the sidewalls is responsible for the cessation of bottom-up filling significantly before sidewall impingement at approximately 21000 s. In terms of the underlying Bi coverage, the lower diffusion coefficient steepens the $\text{Au}(\text{SO}_3)_2^{3-}$ concentration gradient associated with passive deposition, accelerating Bi^{3+} adsorption and thereby shortening (as per Eq. 6) the incubation period preceding activation of deposition at the trench bottom. Activation of the bottom surface itself steepens the gradient further, the concentration at the trench bottom falling below 40 % of the bulk value. This in turn enhances Bi^{3+} adsorption and thus active deposition on the sidewalls, which brings the $\text{Au}(\text{SO}_3)_2^{3-}$ concentration below the activated region essentially to 0 %. The resulting increase of the adsorption kinetics yields a rapid increase of Bi coverage, already substantial over the entire surface in the lower region by 18000 s. However, with deposition at the bottom halted by the absence of metal ions, deposition on the upper active regions

of the sidewalls continues until impingement truncates the feature filling. The activation of deposition on the sidewall area manifests in increase of the current beyond $-20 \mu\text{A}\cdot\text{m}^{-1}$ ($-1 \text{ mA}\cdot\text{cm}^{-2}$) that follows the inflection in the current transient. The current derived from sidewall deposition adds to the current associated with activation of the bottom surface that induced it. Impingement of the sidewall deposits underlies the final decline. Consistent with the parameter changes, deposition on the sidewalls along the occluded void is substantially reduced. The sensitivity of feature filling simulation to electrolyte properties such as metal ion diffusion, conductivity, viscosity, etc., speaks to the need for direct measurement of these quantities to further refine their contributions to the feature filling dynamics.

DISCUSSION

The bottom-up filling mechanism detailed herein includes a combination of features. Adsorbate enrichment with area reduction, the CEAC mechanism, has previously been utilized to describe superconformal metal deposition from accelerated electrolytes with substantial success.^{30-32,40-45} The accelerator-based model implemented here reflects the superior surfactant quality of the activating species at dilute coverage, undergoing deactivation as a higher order reaction in the adsorbate coverage and thereby damping the approach to higher values of coverage. Adsorption and desorption as expressed here are characteristic of standard Langmuir adsorption models, albeit the kinetic prefactor for the adsorption term is modified in accord with experimental observation. The variation of incubation times on RDE with $\text{Au}(\text{SO}_3)_2^{3-}$ and SO_3^{2-} concentrations is, by itself, consistent with modestly faster deposition on recessed surfaces due to accelerated Bi^{3+} adsorption derived from depletion gradients associated with Au deposition. The increase of incubation times at more positive potentials is consistent with direct measurements of Bi^{3+} adsorption.² The

simulations obtained from the resulting model capture not only the bottom-up filling of high aspect ratio recessed features that is of practical interest but also the incubation period that precedes the filling evolution and the self-passivation upon approach to planarity that follows it. The experimentally observed transition from subconformal, truncated bottom-up filling to bottom-up filling to conformal filling that occurs as the applied potential is shifted positive is also captured by the model with a single parameter set. These are viewed as a substantial result given the experimental basis and simplicity of the model.

Differences such as those in the current transients associated with feature filling simulations as compared to experiment highlight some of the assumptions made in formulating the model as well as in estimating parameters for it. Among these, the evolution of Bi adsorption need not be impacted by potential and concentration solely through the adsorption kinetics as expressed in Eq. 6, and the deposition rate versus adsorbate coverage dependence adopted in Eq. 14 is but one of an infinite variety that exhibit a transition between two states at nonzero value of the input parameter. Estimation of the active and passive deposition rates at -0.72 V from voltammetry and other measurements was discussed previously; other values in Table I lack even such an approximate basis. The transport parameters in Table I represent only physically reasonable values, pending better description or measurements. Indeed, as suggested by the simulation, the lower value of D_{Au} used for **Fig. 11** could very well be more appropriate than that in Table I. As such, one might consider fitting of the feature filling experiments themselves to evaluate the model parameters. However, such an approach comes with a caveat regarding uniqueness. As just one example, deposition fast enough to tax metal ion transport can alternatively be obtained by lowering k_{des}/k_+^0 and k_{bur}/k_+^0 or raising j_1^0 , either of which would increase the concentration gradient by increasing the active deposition rate. Some values might be reasonably be excluded;

these same changes would decrease incubation periods and bottom-up filling times that, already noted for the values in Table I, are modestly shorter than experiment. Uncertainty remains however in that some parameters can be adjusted together, e.g., one increased while another is decreased, for example k_{des}/k_+^0 and k_{bur}/k_+^0 , such that the model still exhibits the most significant experimental findings.

Even the analysis of independent measurements comes with caveats. The rather low value of $\alpha_0 = 0.2$ obtained from the potential dependence of the passive state in the negative-going scans in voltammetry could reflect significant contributions from a parasitic process. In fact, current densities of approximately (-0.8, -0.5 and -0.3) mA·cm⁻² during the incubation period at (-0.76, -0.74 and -0.72) V in the 60 μm deep, 1 μm wide, 2 μm pitch trenches in **Fig. 10** (as well as Fig. 15 in Ref. 6) suggest that $\alpha_0 = 0.6$ might provide a better description. Additional measurements, preferably also at the more positive potentials relevant to filling of the tallest and highest aspect ratio features, are needed to more firmly ground the formalism and associated kinetics.

Although not considered in the model, a subset of the experimental work suggests that pH plays a measurable role in the kinetics of Au deposition. The influence of gradients of pH on suppressor action in ferrous electrolytes has previously been discussed in the context of superconformal Co and Co-Fe deposition in damascene features.⁵⁶ More recent studies^{57,58} examined the impact of pH on superconformal Co deposition through its impact on additive adsorption in the context of implementation in microelectronics manufacture. The role of pH in actual feature filling has also been explicitly modeled for NDR-based Cu filling of microvias, in particular through its impact on carrier concentration and electrical conductivity.⁵⁹ In the gold sulfite electrolytes used in the present study the homogenous sulfite/bisulfite equilibria might be expected to modestly impact

local pH through scavenging of H^+ by the SO_3^{2-} released during reduction of the $Au(SO_3)_2^{3-}$ complex to form bisulfate HSO_3^- . The resulting pH gradient might contribute to superconformal filling observed in this system given that previously published results demonstrate incubation times decrease, and thus Bi^{3+} adsorption kinetics presumably increase, as pH increases from 9.5 to 10.3 to 11.5.⁴ At the pH used in this work the Bi^{3+} species are subject to hydrolysis, and hydrox ligands, $BiOH^{2+}$, etc. are involved in the adsorption process⁶⁰ (although XPS indicated that the relevant adsorbed accelerating species is in the metallic form²). However, incubation data analogous to that in **Fig. 1** (not shown here) indicates that the impact of pH around the pH 9 value being considered is not significant, and thus pH was not considered further in the modeling of bottom-up Au trench filling.

In summary, measurements of concentration-dependent activation times on planar substrates provide a clear path for understanding the impact of processing parameters, potential, electrolyte concentrations, etc., on Bi^{3+} -activated superconformal bottom-up Au filling of recessed features in near-neutral, alkaline sulfite electrolytes. The CEAC-based model incorporating Bi adsorption kinetics, in combination with a non-linear dependence of the deposition rate on coverage, captures the critical characteristic of bottom-up superfilling. A threshold Bi coverage is associated with activation of the Au deposition process at the trench bottom while coverage on the field and sidewalls of tall features remains well below the threshold value. The model captures the incubation period followed by the onset and propagation of bottom-up filling that eventually self-terminates as the growth front approaches the free surface, finishing with passivation across the entire workpiece surface.

CONCLUSION

A physical model of Au deposition utilizing measurement-based kinetics from gold-sulfite electrolyte containing Bi^{3+} additive has been developed. It captures the impact of concentration gradients as well as area-change based enhancement of the surfactant Bi adsorbate coverage that localize active deposition to the feature bottom as per the previously detailed CEAC mechanism. Consistent with previous models of superconformally depositing electrolytes containing accelerating and/or suppressing additives, the model assumes additive adsorption occurs at a rate that is proportional to the local additive concentration. Desorption proportional to adsorbate coverage is presumed as is burial in the deposit of insufficiently mobile adsorbate clusters through a quadratic dependence on coverage. Experimental measurements of the incubation period motivated use of a nonlinear dependence of deposition rate on adsorbate coverage as well as adsorption kinetics scaling inversely with both the local metal ion and sulfite concentrations and increasing exponentially with overpotential. Simulations show that concentration gradients arising from deposition in high aspect ratio trenches along with concentration-dependent adsorption kinetics accentuate Bi adsorption farther from feature openings and, in conjunction with decreasing surface area at the trench bottom during metal deposition, through the CEAC mechanism result in an increase of the local coverage of the surfactant accelerating Bi and activation of bottom-up trench filling. As filling proceeds an imbalance of decreasing Bi^{3+} adsorption kinetics versus adsorbate desorption and burial on the evolving interface is responsible for self-passivation as filling approaches the field. In summary, the simulations replicate key experimental observations including the incubation period, localized deposition toward the feature bottom and bottom-up filling and the self-passivation that follows as well as trends of filling geometry with potential, supporting the proposed mechanism of bottom-up Au filling in this system.

ACKNOWLEDGMENTS

Identification of commercial products in this paper is done to specify the experimental procedure. In no case does this imply endorsement or recommendation by the National Institute of Standards and Technology (NIST).

Table I. Parameters for bottom-up Au trench filling simulations

| Parameter | Name | Units | Value |
|--|------------------------|--|----------------------|
| <i>Electrochemical Cell Geometry</i> | | | |
| Trench width | W | μm | 1 |
| Trench height | H | μm | As indicated |
| Trench pitch | P | μm | 2 |
| Boundary layer thickness | δ | μm | 10 |
| Reference/counter electrode distance | $L_{RE} + \delta$ | cm | 2 |
| <i>Electrolyte</i> | | | |
| Bulk concentration $\text{Au}(\text{SO}_3)_2^{3-}$ | C_{Au}^o | $\text{mmol}\cdot\text{L}^{-1}$ | 160 |
| Bulk concentration SO_3^{2-} | C_{Cl}^o | $\text{mmol}\cdot\text{L}^{-1}$ | 640 |
| Bulk concentration Na^+ | C_{Na}^o | $\text{mmol}\cdot\text{L}^{-1}$ | 1760 |
| Bulk concentration Bi^{3+} | C_{Bi}^o | $\mu\text{mol}\cdot\text{L}^{-1}$ | 50 |
| Diffusion coefficient $\text{Au}(\text{SO}_3)_2^{3-}$ | D_{Au} | $\text{cm}^2\cdot\text{s}^{-1}$ | 5×10^{-6} |
| Diffusion coefficient SO_3^{2-} | D_{SO_3} | $\text{cm}^2\cdot\text{s}^{-1}$ | 5×10^{-6} |
| Diffusion coefficient Na^+ | D_{Na} | $\text{cm}^2\cdot\text{s}^{-1}$ | 5×10^{-6} |
| Diffusion coefficient Bi^{3+} | D_{Bi} | $\text{cm}^2\cdot\text{s}^{-1}$ | 5×10^{-6} |
| Ionic charge of gold ion $\text{Au}(\text{SO}_3)_2^{3-}$ | z_{Au} | – | -3 |
| Ionic charge of Bismuth ion Bi^{3+} | z_{Bi} | – | 3 |
| Ionic charge of sulfite ion SO_3^{2-} | z_{SO_3} | – | -2 |
| Ionic charge of sodium ion Na^+ | z_{Na} | – | 1 |
| Electrolyte conductivity | κ | $\text{S}\cdot\text{m}^{-1}$ | 10 |
| <i>Adsorbate</i> | | | |
| Saturation Bi coverage | Γ_{Bi} | $\text{mol}\cdot\text{m}^{-2}$ | 1×10^{-5} |
| Bi adsorption kinetics prefactor | k_+^0 | $\text{m}^3\cdot\text{mol}^{-1}\cdot\text{s}^{-1}$ | 3×10^{-4} |
| Bi desorption kinetics prefactor | k_{Des}^- | s^{-1} | 1×10^{-4} |
| Bi deactivation kinetics prefactor | k_{Bur}^- | m^{-1} | 1×10^7 |
| <i>Electrochemical Kinetics</i> | | | |
| Exchange current density Bi-free surface | j_0^o | $\text{A}\cdot\text{m}^{-2}$ | 2.8×10^{-3} |
| Exchange current density activated surface | j_1^o | $\text{A}\cdot\text{m}^{-2}$ | 6×10^{-2} |
| Charge transfer coefficient Bi-free surface | α_0 | – | 0.2 |
| Charge transfer coefficient activated surface | α_1 | – | 0.5 |
| Au ionic charge for deposition | n | – | 1 |
| Surface diffusion coefficient | $D_{\text{s,Bi}}$ | $\text{cm}^2\cdot\text{s}^{-1}$ | 1×10^{-12} |
| <i>Miscellaneous</i> | | | |
| Au molar volume | Ω | $\text{cm}^3\cdot\text{mol}^{-1}$ | 10.2 |
| Applied potential | V_{app} | V | As indicated |
| Equilibrium potential | E_{eq} | V | -0.4 |
| Critical Coverage | θ_{crit} | – | 0.15 |
| Activation Range | $\Delta\theta$ | – | 0.02 |
| Faraday's Constant | F | $\text{C}\cdot\text{mol}^{-1}$ | 96485 |
| Temperature | T | K | 293 |

REFERENCES

1. D. Josell and T. P. Moffat, *J. Electrochem. Soc.*, **166**, D3022 (2019).
2. S. Ambrozik, T.P. Moffat, C. Zhang, H. Miao and D. Josell, *J. Electrochem. Soc.*, **166**, D443 (2019).
3. D. Josell, M. Williams, S. Ambrozik, C. Zhang and T.P. Moffat, *J. Electrochem. Soc.*, **166**, D487 (2019).
4. D. Josell, S. Ambrozik, M.E. Williams, A.E. Hollowell, C. Arrington, S. Muramoto and T.P. Moffat, *J. Electrochem. Soc.*, **166**, D898 (2019).
5. D. Josell, Z. Shi, K. Jefimovs, L. Romano, M. Stampanoni and T. P. Moffat, *J. Electrochem. Soc.*, **167**, 132504 (2020).
6. D. Josell, Z. Shi, K. Jefimovs, V. A. Guzenko, C. Beauchamp, L. Peer, M. Polikarpov and T. P. Moffat, *J. Electrochem. Soc.*, **168**, 082508 (2021).
7. D. Josell, W. Osborn, M.E. Williams and H. Miao, *J. Electrochem. Soc.*, **169**, 032509, (2022).
8. Z. Shi, D. Josell, K. Jefimovs, L. Romano, T. P. Moffat, M. Stampanoni and C. M. Schlepütz, *Appl. Opt.*, **61**, 3850 (2022).
9. S. Rutishauser, L. Samoylova, J. Krzywinski, O. Bunk, J. Grünert, H. Sinn, M. Cammarata, D. M. Fritz, and C. David, *Nat. Commun.*, **3**, 947 (2012).
10. T. Weitkamp, A. Diaz, C. David, F. Pfeiffer, M. Stampanoni, P. Cloetens and E. Ziegler, *Opt. Express*, **13**, 6296 (2005).

11. I. Zanette, T. Weitkamp, T. Donath, S. Rutishauser, and C. David, *Phys. Rev. Lett.*, **105**, 248102 (2010).
12. Y.W. Liu, M. Seaberg, D.L. Zhu, J. Krzywinski, F. Seiboth, C. Hardin, D. Cocco, A. Aquila, B. Nagler, H.J. Lee, S. Boutet, Y.P. Feng, Y.T. Ding, G. Marcus, and A. Sakdinawat, *Optica*, **5**, 967 (2018).
13. P. Emma, R. Akre, J. Arthur, R. Bionta, C Bostedt, J. Bozek, A. Brachmann, P. Bucksbaum, R. Coffee, F.J. Decker, Y. Ding, D. Dowell, S. Edstrom, A. Fisher, J. Frisch, S. Gilevich, J. Hastings, G. Hays, P. Hering, Z. Huang, R. Iverson, H. Loos, M. Messerschmidt, A. Mtahnahri, S. Moeller, H.D. Nuhn, G. Pile, D. Ratner, J. Rzepiela, D. Schultz, T. Smith, P. Stefan, H. Tompkins, J. Turner, J. Welch, W. White, J. Wu, G. Yocky and J. Galayda, *Nat. Photon.*, **4**, 641 (2010).
14. C. Pellegrini, A. Marinelli, and S. Reiche, *Rev. Mod. Phys.*, **88**, 015006 (2016).
15. A. Snigirev, I. Snigireva, V. Kohn, S. Kuznetsov and I. Schelokov, *Rev. Sci. Instrum.*, **66**, 5486 (1995).
16. J. Vila-Comamala, L. Romano, K. Jefimovs, H. Dejea, A. Bonnin, A. C. Cook, I. Planinc, M. Cikes, Z. Wang, and M. Stampanoni, *Opt. Express*, **29**, 2049 (2021).
17. F.T. Gassert, T. Urban, M. Frank, K. Willer, W. Noichl, P. Buchberger, R. Schick, T. Koehler, J. von Berg, A.A. Fingerle, A.P. Sauter, M.R. Makowski, D. Pfeiffer and F. Pfeiffer, *Radiology*, **301**, 389 (2021).
18. K. Willer, A.A. Fingerle, W. Noichl, F. De Marco, M. Frank, T. Urban, R. Schick, A. Gustschin, B. Gleich, J. Herzen, T. Koehler, A. Yaroshenko, T. Pralow, G.S. Zimmermann, B.

Renger, A.P. Sauter, D. Pfeiffer, M.R. Makowski, E.J. Rummeny, P.A. Grenier and F. Pfeiffer, L. *Digit. Health*, **3**, e733 (2021).

19. A.P. Sauter, J. Andrejewski, F. De Marco, K. Willer, L.B. Gromann, W. Noichl, F. Kriner, F. Fischer, C. Braun, T. Koehler, F. Meurer, A.A. Fingerle, D. Pfeiffer, E. Rummeny, J. Herzen, and F. Pfeiffer, *Scientific Reports*, **9**, 8699 (2019).

20. C. Arboleda, Z.T. Wang, K. Jefimovs, T. Koehler, U. Van Stevendaal, N. Kuhn, B. David, S. Prevrhal, K. Lang, S. Forte, R.A. Kubik-Huch, C. Leo, G. Singer, M. Marcon, A. Boss, E. Roessl and M. Stampanoni, *European Radiology*, **30**, 1419 (2020).

21. J. Andrejewski, F. de Marco, K. Willer, W. Noichl, A. Gustschin, T. Koehler, P. Meyer, F. Kriner, F. Fischer, C. Braun, A.A. Fingerle, J. Herzen, F. Pfeiffer and D. Pfeiffer, *European Radiology Experimental*, **5**, 6 (2021).

22. R.J. Morrissey, *Plating Surf. Finish.*, **80**, 75 (1993).

23. J.-Q. Yang, L. Jin, Y.-H. Xiao, H.-H. Yu, F.-Z. Yang, D.-P. Zhan, D.-Y. Wu and Z.-Q. Tian, *Langmuir*, **37**, 11251 (2021).

24. J.D.E. McIntyre and W.F. Peck, *J. Electrochem. Soc.*, **123**, 1800, (1976).

25. H. Honma and Y. Kagaya, *J. Electrochem. Soc.*, **140**, L135 (1993).

26. T. Osaka, A. Kodera, T. Misato, T. Homma, Y. Okinaka, and O. Yoshioka *J. Electrochem. Soc.*, **144**, 3462 (1997).

27. Y. Okinaka and M. Hoshino, *Gold Bulletin*, **31**, 3 (1998).

28. T.A. Green and S. Roy, *J. Electrochem. Soc.*, **153**, C157 (2006).

29. T. A. Green, *Gold Bulletin*, **40**, 105 (2007).
30. D. Josell, C.R. Beauchamp, D.R. Kelley, C.A. Witt and T.P. Moffat, *Electrochem. Solid-State Lett.*, **8**, C54 (2005).
31. D. Josell, D. Wheeler and T.P. Moffat, *J. Electrochem. Soc.*, **153**, C11 (2006).
32. D. Josell and T.P. Moffat, *J. Electrochem. Soc.*, **160**, D3009 (2013).
33. N. Shirai, S. I. Yoshimura, E. Sato and N. Kubota, *J. Surf. Finish. Soc. Jap.*, **40**, 543 (1989).
34. T. P. Moffat and D. Josell, *J. Electrochem. Soc.*, **159**, D208 (2012).
35. D. Josell, D. Wheeler, T. P. Moffat, *J. Electrochem. Soc.*, **159**, D570 (2012).
36. D. Wheeler, D. Josell and T.P. Moffat, *J. Electrochem. Soc.*, **160**, D3260 (2013).
37. D. Josell and T.P. Moffat, *J. Electrochem. Soc.*, **160**, D3035 (2013).
38. D. Josell and T.P. Moffat, *J. Electrochem. Soc.*, **164**, D327 (2017).
39. D. Josell and T.P. Moffat, *J. Electrochem. Soc.*, **168**, 052502 (2021).
40. T.P. Moffat, D. Wheeler, W.H. Huber, and D. Josell, *Electrochem. Solid-State Lett.*, **4**, C26 (2001).
41. D. Josell, D. Wheeler, W.H. Huber, J.E. Bonevich and T.P. Moffat, *J. Electrochem. Soc.*, **148**, C767 (2001).
42. D. Wheeler, D. Josell and T.P. Moffat, *J. Electrochem. Soc.*, **150**, C302 (2003).
43. D. Josell, T.P. Moffat, D. Wheeler, *J. Electrochem. Soc.*, **151**, C19 (2004).
44. T. P. Moffat, D. Wheeler, M.D. Edelstein and D. Josell, *IBM J. Res. Dev.*, **49**, 19 (2005).

45. D. Josell, T.P. Moffat and D. Wheeler, *J. Electrochem. Soc.*, **154**, D208 (2007).
46. Binary Alloy Phase Diagrams, 2nd Edition, Vol. 1, Eds. T. B. Massalsky, H. Okamoto, P.R. Bhubramanian and L. Kacprzak, pp. 343-346 (ASM International, Materials Park, OH) 1990.
47. J. Tersoff, *Phys. Rev. Lett.*, **74**, 434 (1995).
48. C.-H. Chen, A.A. Gewirth, *J. Am. Chem. Soc.*, **114**, 5439 (1992).
49. C.-H. Chen, K.D. Kepler, A.A. Gewirth, B.M. Ocko, J. Wang, *J. Phys. Chem.*, **97**, 7290 (1993).
50. I. Oh, M.E. Biggin, A.A. Gewirth, *Langmuir*, **16**, 1397 (2000).
51. K. Tamura, B. M. Ocko, J.X. Wang, R.R. Adzic, *J. Phys. Chem. B.*, **106**, 3896 (2002).
52. M. Hara, Y. Nagahara, S. Yoshimoto, J. Inukai, K. Itaya, *J. Electrochem. Soc.*, **151**, 91 (2004).
53. M. Hara, Y. Nagahara, J. Inukai, S. Yoshimoto, K. Itaya, *Electrochim. Acta*, **51**, 2327 (2006).
54. J.P. Monochoux, D. Chatain, P. Wynblatt, *Surf. Sci.*, **600**, 1265 (2006).
55. R. van Gastel, D. Kaminski, E. Vlieg, B. Poelsema, *Surf. Sci.*, **603**, 3292 (2009).
56. C. H. Lee, J. E. Bonevich, J. E. Davies and T.P. Moffat, *J. Electrochem. Soc.*, **156**, D301 (2009).
57. J. Wu, F. Wafula, S. Branagan, H. Suzuki and J. van Eizden, *J. Electrochem. Soc.*, **166**, D3136 (2019).
58. M. A. Rigsby, L. J. Brogan, N. V. Doubina, Y. Liu, E. C. Opocensky, T. A. Spurlin, J. Zhou and J. D. Reid, *J. Electrochem. Soc.*, **166**, D3167 (2019).

59. T. M. Braun, J. John, N. Jayaraju, D. Josell and T. P. Moffat, *J. Electrochem. Soc.*, **169**, 012502 (2022).

60. N.A. Rogozhnikov, *Russ. J. Electrochem.*, **54**, 1201 (2018).

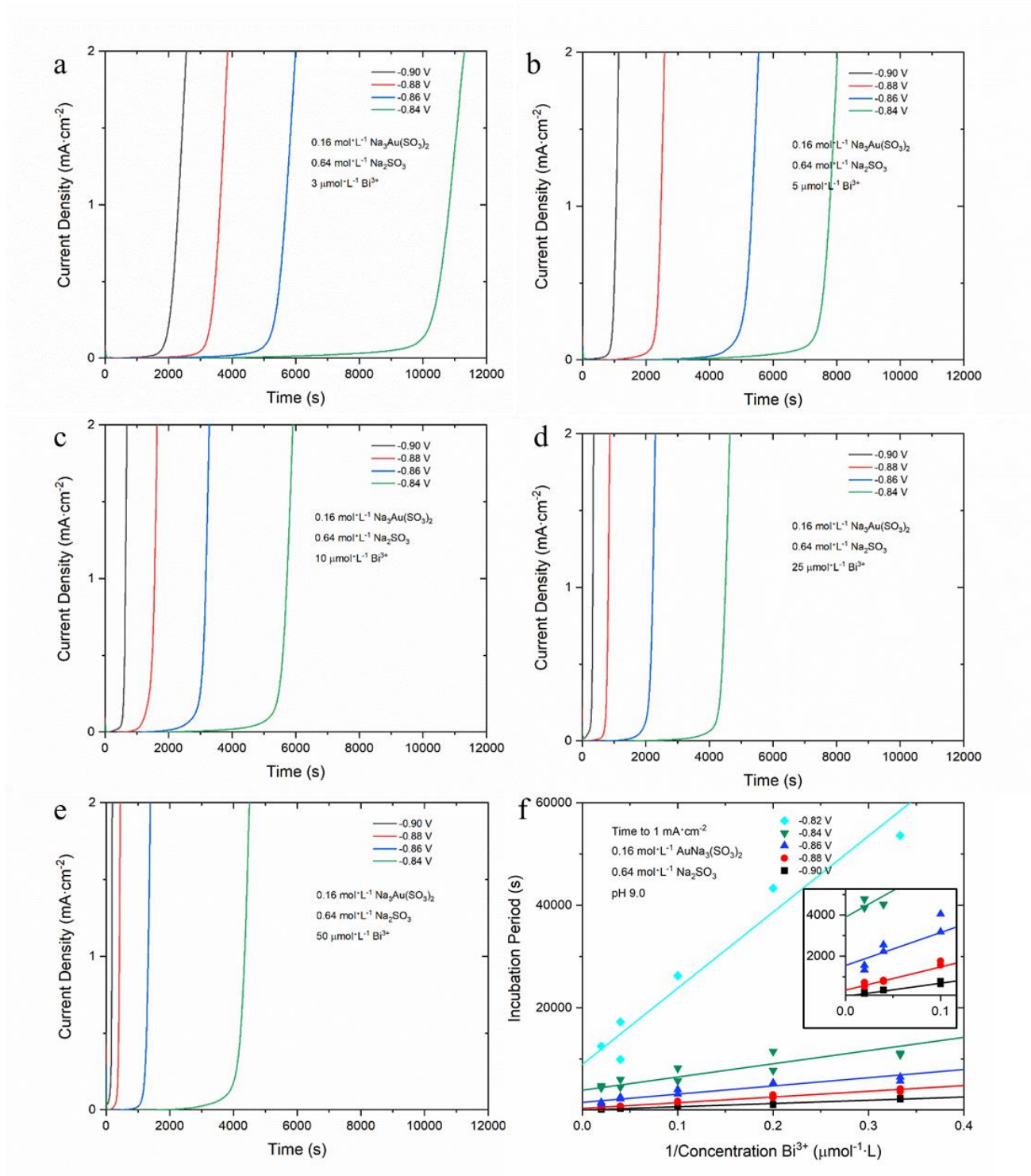


Figure 1: Chronoamperometry for reductive Au deposition at the indicated potentials in 0.16 mol·L⁻¹ Na₃Au(SO₃)₂+0.64 mol·L⁻¹ Na₂SO₃ electrolyte of pH 9.0 containing a) 3 μmol·L⁻¹ Bi³⁺,

b) $5 \mu\text{mol}\cdot\text{L}^{-1} \text{Bi}^{3+}$, c) $10 \mu\text{mol}\cdot\text{L}^{-1} \text{Bi}^{3+}$, d) $25 \mu\text{mol}\cdot\text{L}^{-1} \text{Bi}^{3+}$ and e) $50 \mu\text{mol}\cdot\text{L}^{-1} \text{Bi}^{3+}$. f) Summary of the incubation time to reach $1 \text{ mA}\cdot\text{cm}^{-2}$ as a function of the Bi^{3+} concentration with linear fits to $1/\text{Bi}^{3+}$ at each potential; inset shows intercepts near the origin. The RDE was rotating at 100 rpm ($200\pi \text{ rad}\cdot\text{min}^{-1}$), data was acquired without compensation for the (9 to 11) Ω cell resistance, and current density is obtained by normalizing the measured current to the nominal projected electrode area of the 0.5 cm diameter RDE.

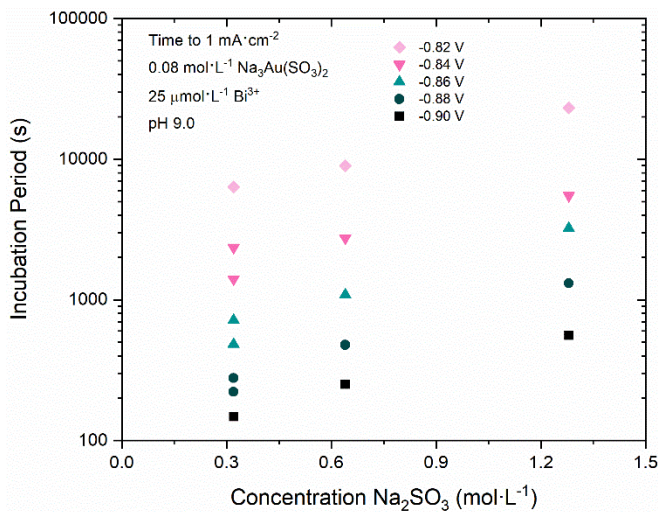
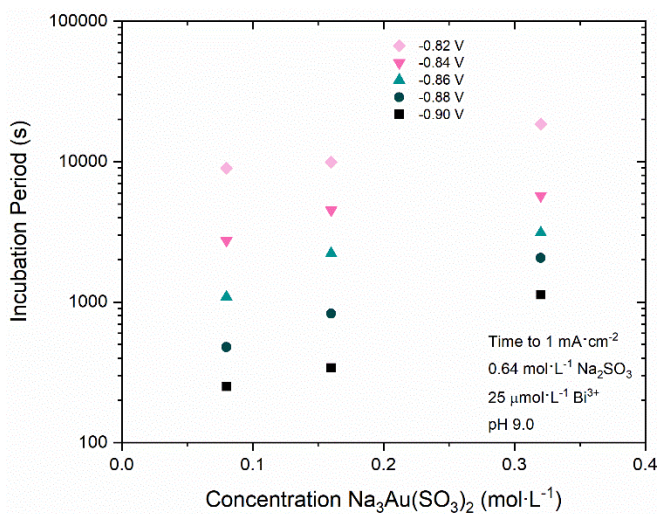


Figure 2: Incubation periods defined by the time required for current transients to reach $1 \text{ mA}\cdot\text{cm}^{-2}$ at the indicated potentials in different electrolytes: Top) $0.64 \text{ mol}\cdot\text{L}^{-1} \text{ Na}_2\text{SO}_3$ with variable $\text{Na}_3\text{Au}(\text{SO}_3)_2$ concentration and bottom) $0.08 \text{ mol}\cdot\text{L}^{-1} \text{ Na}_3\text{Au}(\text{SO}_3)_2$ with variable Na_2SO_3 concentration. All electrolytes are of pH 9.0 and contain $25 \text{ }\mu\text{mol}\cdot\text{L}^{-1} \text{ Bi}^{3+}$. The RDE was rotated at 100 rpm, and data was acquired without compensation for the (9 to 11) Ω cell resistance. The current density was evaluated based on the nominal projected area of the 0.5 cm diameter RDE.

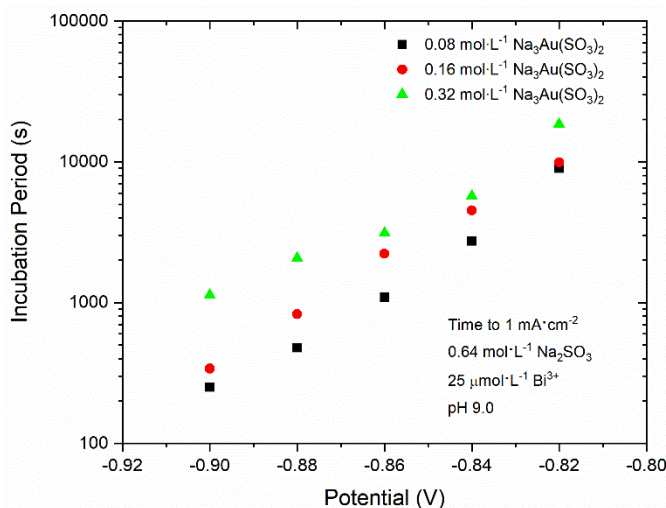


Fig. 3: The potential dependence of the incubation period based on time required for current transients to reach $1 \text{ mA}\cdot\text{cm}^{-2}$ in electrolytes of pH 9.0 composed of $x \text{ mol}\cdot\text{L}^{-1} \text{ Na}_3\text{Au}(\text{SO}_3)_2 + 0.64 \text{ mol}\cdot\text{L}^{-1} \text{ Na}_2\text{SO}_3$ and $25 \text{ }\mu\text{mol}\cdot\text{L}^{-1} \text{ Bi}^{3+}$, with values x as indicated. The RDE was rotated at 100 rpm, and data was acquired without compensation for the (9 to 11) Ω cell resistance. The current density was evaluated based on the nominal projected area of the 0.5 cm diameter RDE.

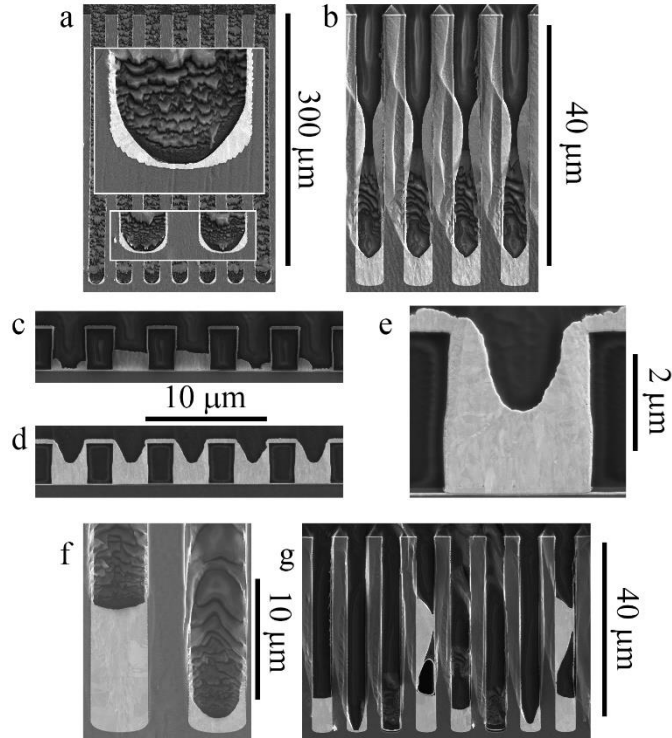


Fig. 4: Profiles indicative of Au deposition initiating at the corners where sidewalls meet trench bottoms in: a) 305 μm deep trenches with atomic layer deposited Pt seed layer, including inserts at higher magnifications, b) 45 μm deep trenches with evaporated Au seed layer, exhibiting wedge shaped lower profile (as well as imminent truncation due to activation on the sidewall above), c) 3 μm deep trenches, with sputter deposited Au seed layer on non-silicon dielectric sidewalls, exhibiting irregular initiation at lower corners, d) 3 μm deep trenches with freshly evaporated Au layer on sputter deposited Au seed layer, exhibiting superconformal filling more suggestive of CEAC-based evolution, e) a higher magnification view of the same, f-g) 45 μm deep trenches with evaporated Au seed layer, exhibiting wedge-shaped lower profiles (irregular filling caused by poorly controlled electrical contact to the field between trenches). Electrolytes and deposition conditions vary.

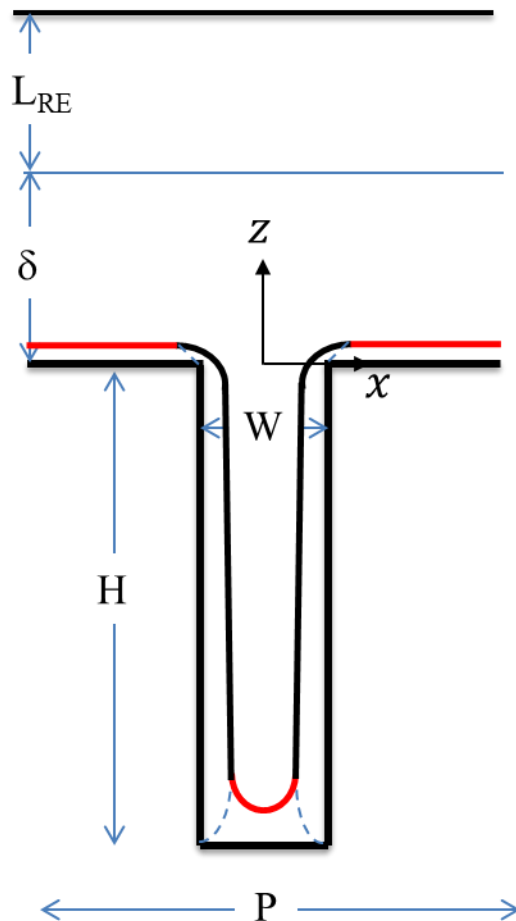


Fig. 5: Schematic of original two-dimensional trench geometry as well as the domain remaining unfilled at nonzero time characterized by the simulations of Au deposition. The electrolyte is stationary, with diffusion from the bulk concentration across the boundary layer of thickness δ and potential drop through the electrolyte across the distance $L_{RE} + \delta$ from the reference electrode (not drawn to scale, $L_{RE} \gg \delta$). Relevant boundaries and dimensions are labeled. Adsorbate coverage on, as well as electrolyte concentrations adjacent to, the field and bottom are evaluated along the red segments defined by growth from the upper and lower corners along the dashed lines. Values for dimensions and other parameters are as stated in Table I unless otherwise indicated.

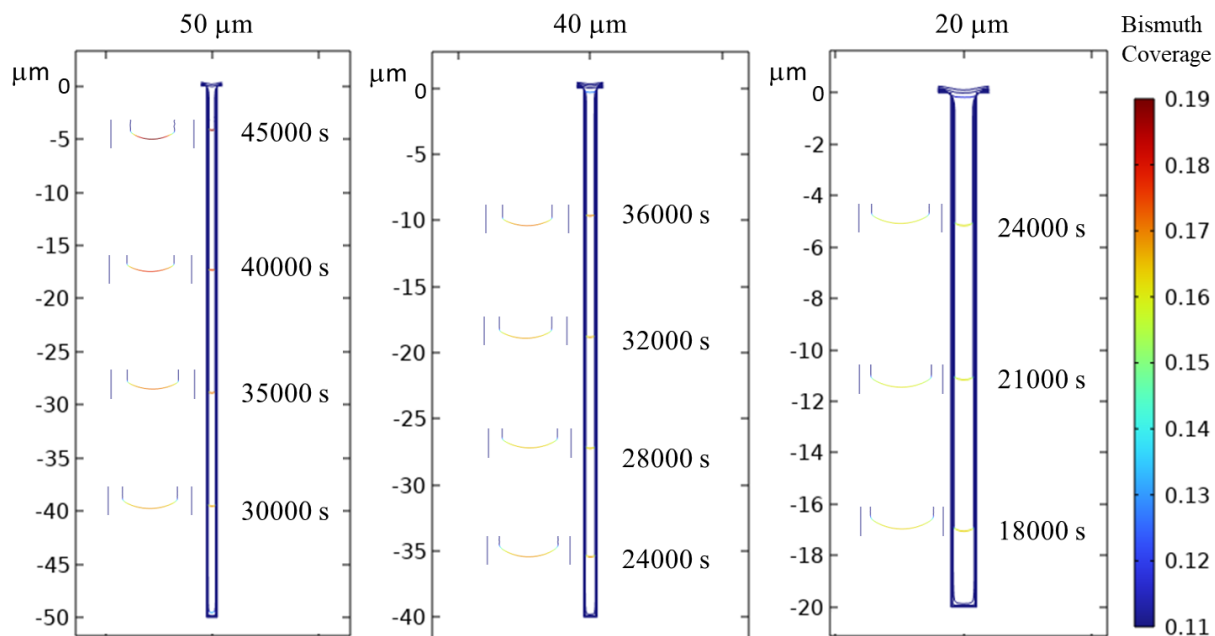


Fig. 6: Simulations of Au deposition in 1 μm wide trenches of 50 μm , 40 μm and 20 μm depth, all at 2 μm pitch and for deposition at -0.72 V. Growth contours are shown from 0 s to 60000 s at 5000 s intervals, from 0 s to 52000 s at 4000 s intervals, and from 0 s to 33000 s at 3000 s intervals, respectively, and are colored according to local Bi coverage as defined by the color bar on the right. Deposition times are indicated next to the profiles located within the body of the trench that are associated with the period of active bottom-up filling (i.e., after the incubation period and prior to the self-passivation) along with inserts of the bottom surface at higher magnification. Parameters for the simulations are found in Table I.

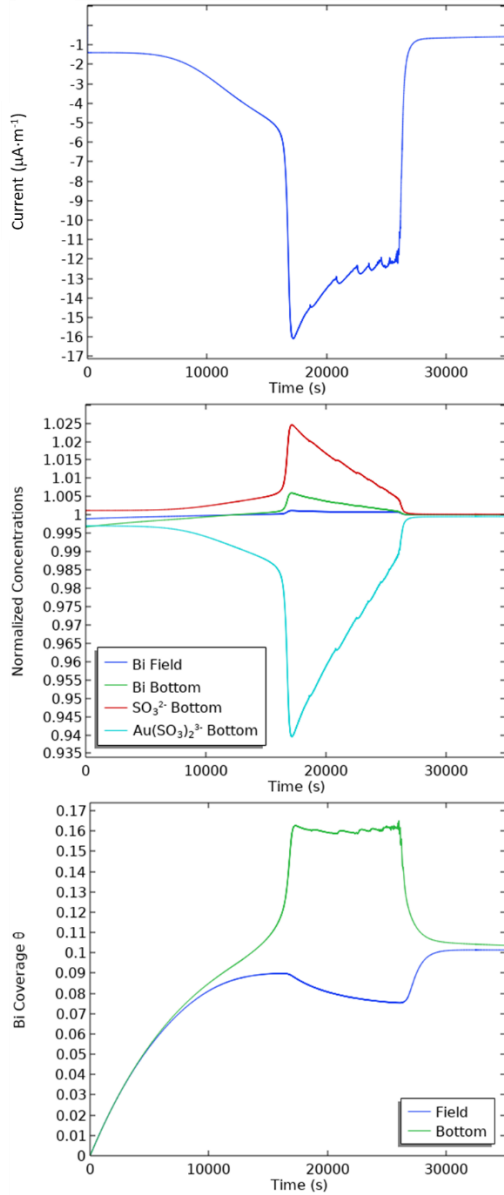


Fig. 7: (Top) Time dependent deposition current, (Middle) concentrations of $\text{Au}(\text{SO}_3)_2^{3-}$, SO_3^{2-} and Bi^{3+} as fractions of bulk values at the indicated locations, see schematic in **Fig. 5**, and (Bottom) fractional adsorbate coverage on the field and bottom of the filling trench for the simulation of deposition in 20 μm deep 1 μm wide trenches at -0.72 V shown in **Fig. 6**. Given the 2 μm pitch of each trench, current density integrated across the profile of the deposit of $20 \mu\text{A}\cdot\text{m}^{-1}$ (current per length of trench) is equivalent to current density of $1 \text{mA}\cdot\text{cm}^{-2}$ (current per planar

projected area of grating). Oscillations in the traces are associated with remeshing actuated automatically with degradation of mesh quality.

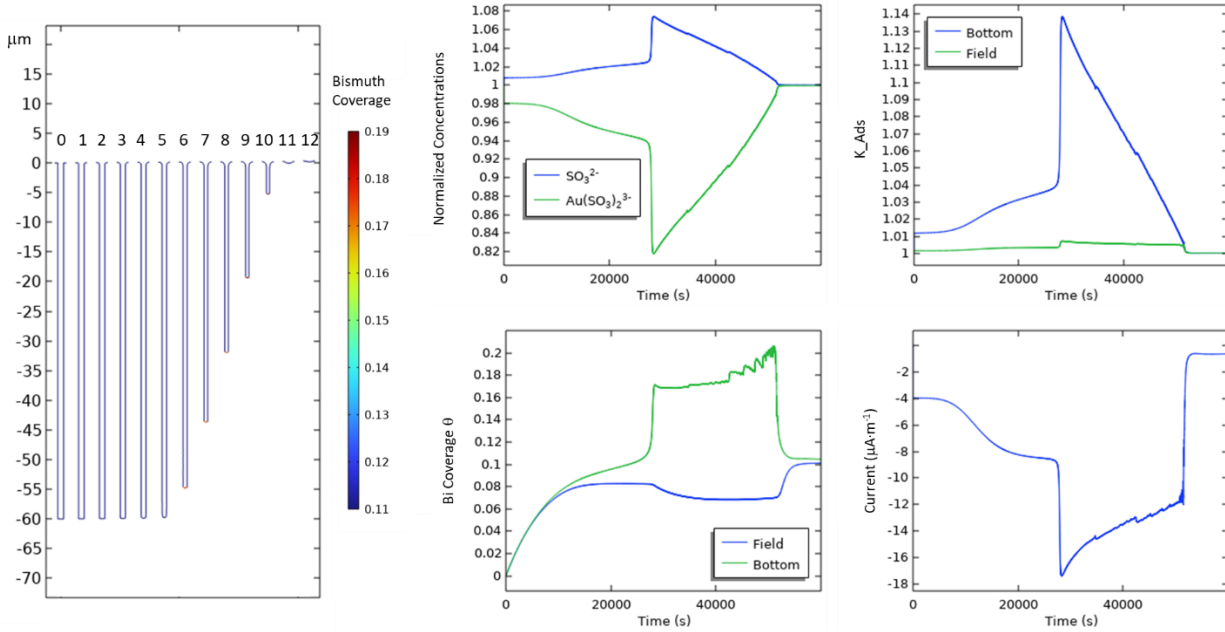


Fig. 8: Simulations of Au deposition in 1 μm wide 60 μm deep trenches at 2 μm pitch during filling at -0.72 V . Fill profiles capturing deposition from 0 s to 60000 s are shown on the left with deposition times specified by the multiple of 5000 s indicated above each. The profiles are colored according to local Bi coverage as defined by the adjacent color bar, with local enhancement evident only along the bottom surface. Other parameters for the simulation are found in Table I. The four accompanying plots show the corresponding time dependent: concentrations of $\text{Au}(\text{SO}_3)_2^{3-}$ and SO_3^{2-} in the electrolyte normalized to bulk values at the bottom of the filling trench (see schematic in **Fig. 5**), concentration- and potential-dependent adsorption kinetic factor k_+ at the bottom of the filling trench and along the field over it normalized to its value in bulk electrolyte at the applied potential, fractional Bi coverage at the same locations and current density integrated across the profile; $20\ \mu\text{A}\cdot\text{m}^{-1}$ (current per length of trench) is equivalent to $1\ \text{mA}\cdot\text{cm}^{-2}$ (current per projected

area of grating) for the 2 μm pitch of the trenches. Oscillations in the traces are associated with remeshing actuated automatically in the software by degradation of mesh quality.

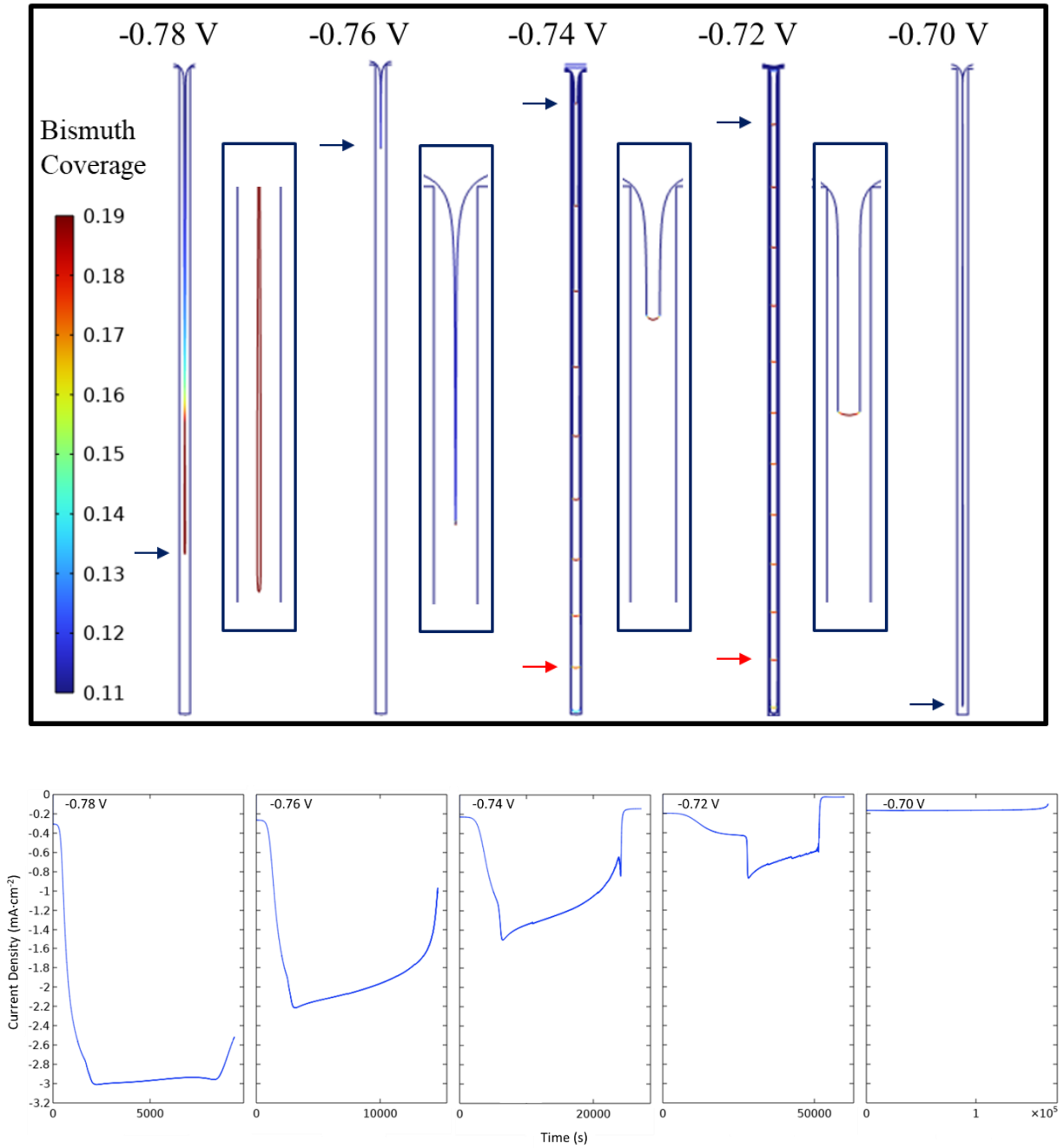


Fig. 9: Simulations of deposition in a 60 μm deep 1 μm wide trench. Boundary conditions are consistent with a periodic array of 2 μm pitch. Surface contours are shown in the trench for: -0.78 V just prior to sidewall impingement and void formation after 9000 s; -0.76 V just prior to sidewall impingement and void formation after 14000 s; -0.74 V at 0 s to 28000 s in 2000 s increments, with fill height at 8000 s that is subsequent to activation indicated (\rightarrow); -0.72 V from 0 s to 60000 s in 2000 s increments, with fill height at 30000 s, subsequent to activation, indicated (\rightarrow); and -0.70 V the central seam at 165000 s. Only final profiles are shown at -0.78 V, -0.76 V and -0.70 V for the sake of visual clarity. Final fill height is indicated for the simulations at -0.78 V, -0.76 V and -0.70 V that failed (\rightarrow), while the final contour of active deposition is indicated for the simulations that bottom-up filled (\rightarrow): 24000 s at -0.74 V and 50000 s at -0.72 V. Higher magnification insets are provided for approximately 9 μm tall sections of the corresponding contours at the more negative potentials. The corresponding current transients normalized to planar projected (i.e., grating) area are shown beneath. Other parameters for the simulation are found in Table I.

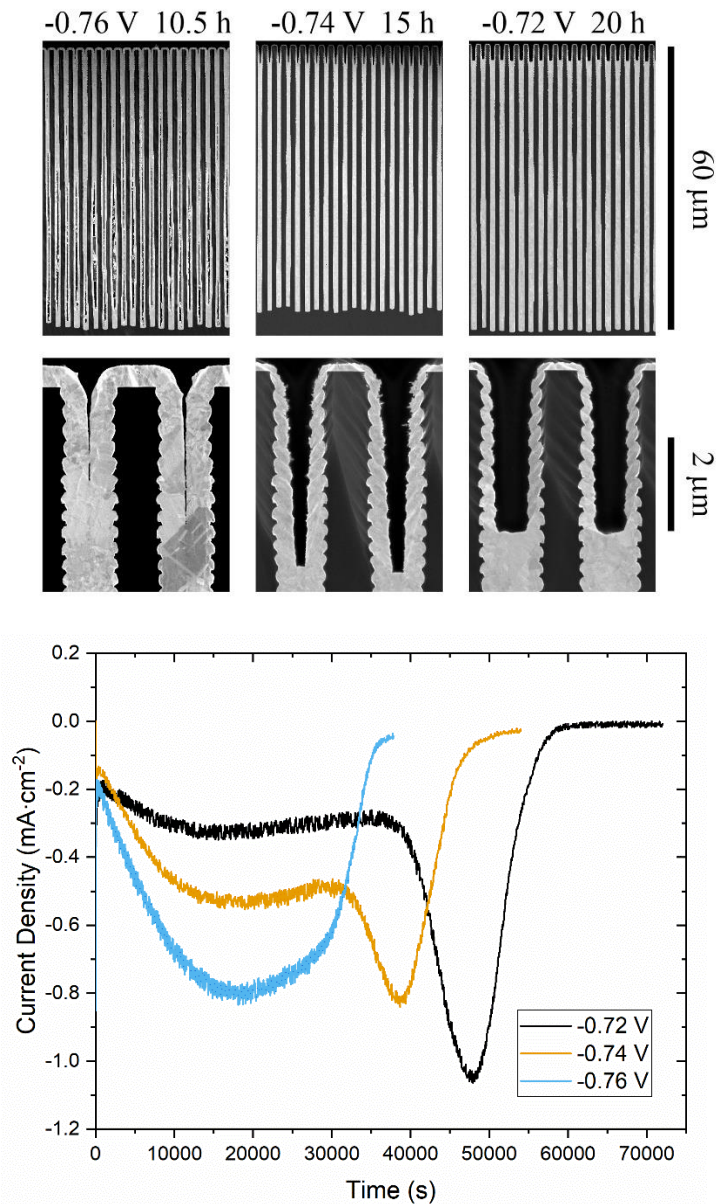


Fig. 10: Top) Scanning electron microscope images of Au electrodeposits in cross-sectioned gratings having trenches that are $\approx 60 \mu\text{m}$ deep and $\approx 1 \mu\text{m}$ wide at $2 \mu\text{m}$ pitch with the deposition potentials and times indicated. Higher magnification images of the respective trench openings are shown beneath. Bottom) Associated current density transients with the measured current normalized to the planar, projected area of the patterned substrate. All specimens were rotated at 200 rpm about the vertical axis with the specimens suspended in $0.16 \text{ mol}\cdot\text{L}^{-1} \text{ Na}_3\text{Au}(\text{SO}_3)_2 + 0.64$

$\text{mol}\cdot\text{L}^{-1}$ Na_2SO_3 electrolyte of pH 9.0 containing $50\ \mu\text{mol}\cdot\text{L}^{-1}$ Bi^{3+} . This configuration ensured that all measured current was associated with deposition in the patterned trench array. Additional details in Ref. 6.

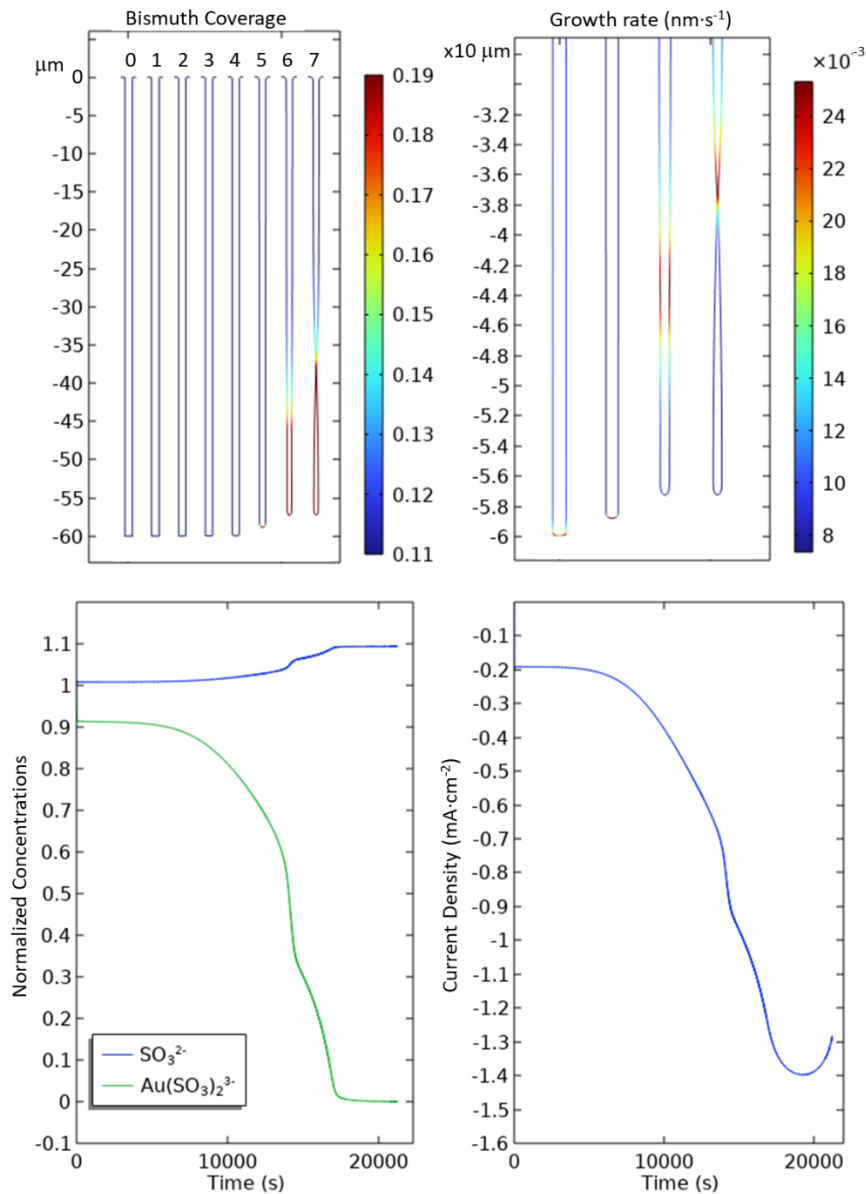


Fig. 11: Simulation of deposition in a 60 μm deep 1 μm wide trench at -0.72 V . Boundary conditions are consistent with a periodic array of 2 μm pitch. The diffusion coefficient for the Au ions D_{Au} of $1 \times 10^{-6}\text{ cm}^2\cdot\text{s}^{-1}$ and electrolyte conductivity κ of $20\text{ S}\cdot\text{m}^{-1}$ differ from those in Table I. Top row) Filling contours for deposition times of 0 s to 21000 s in increments of 3000 s are shown left to right in the plot colored by Bi coverage. The lower portion of the trench in the final four contours is shown in a separate plot colored by deposition rate. The contours are colored

according to local Bi coverage or local deposition rate as stated and defined by the adjacent color bars. Bottom row) Plots of the corresponding concentrations of $Au(SO_3)_2^{3-}$ and SO_3^{2-} in the electrolyte at the bottom of the filling trench (see schematic in **Fig. 5**) and deposition current density integrated across the profile and normalized to planar projected (i.e., grating) area for the 2 μm pitch of the trenches. The code halted upon sidewall impingement.